V_p/V_s structure and P_n anisotropy across the Louisville Ridge, seaward of the Tonga-Kermadec Trench

Eduardo Contreras-Reyes[1], Ingo Grevemeyer[2], Christine Peirce[3], and Sebastián Obando-Orrego[1],

[1]Departamento de Geofísica, Facultad de Ciencias Físicas y Matemáticas, Universidad de Chile, Santiago, Chile

[2]GEOMAR-Helmholtz Centre for Ocean Research, Kiel, Germany

[3]Department of Earth Sciences, Durham University, South Road, Durham, DH1 3LE, UK

Abstract

The Pacific Plate within the collision zone between the Louisville Ridge and the Tonga-Kermadec Trench was formed at the Osbourn Trough, a paleo spreading center that became inactive during the Cretaceous. In this region, the trench shallows from a depth of 8-11 km to ~6 km below sea surface, while the outer rise topography is obscured by Louisville seamounts that rise 4-5 km above the adjacent seafloor. We derive 2-D P-wave (V_p) and S-wave (V_s) velocity-depth models along a wide-angle seismic profile oriented sub-parallel to the trench axis, intersecting the 27.6ºS seamount. The seismic profile is located in the down-going Pacific Plate eastwards from the trench axis (~100 km distant at the south end and ~150 km at the north end), where bending-related faulting is limited or absent. Using the derived P- and S-wave velocity-depth models we calculate the corresponding V_p/V_s ratio model which shows values of 1.7-1.85 throughout the oceanic crust either side of the Louisville Ridge where it is unaffected by magmatism associated with its formation. This range of observations lies within those documented by laboratory measurements on basalt, diabase, and gabbro. Conversely, in the vicinity of the summit of 27.6ºS seamount, the relatively elevated V_p/V_s (~1.9) ratio observed can be attributed to water-saturated cracks within the shallow sub-seabed section of the intrusive core. Beneath the seamount the uppermost mantle has a V_p ranging from 8.0 to 8.9 km/s. Comparing our P-wave model with a pre-existing model running sub-perpendicularly along the Louisville Ridge axis, we observe an anisotropy of up to ~6% at a depth of 3-4 km below the Moho. The predominant

orientation of the faster axis follows the direction of paleo spreading flow when the plate was formed at the Osbourn Trough.

Key Points:

- We obtain a V_p/V_s ratio of ~1.9 near the summit of the 27.6ºS seamount.
- We find mean V_p/V_s ratios of 1.7-1.85 for the oceanic crust adjacent to the Louisville Ridge.
- Seismic anisotropy of up to 6% is observed in the upper 15 km of the mantle.

1. Introduction

Oceanic hotspot magmatism results from the dynamic interaction between an overlying oceanic tectonic plate and an ascending, thermally buoyant mantle plume originating in the Earth's deeper mantle. Ridges that form along oceanic hotspot tracks far from a spreading center (off-ridge setting) are generally characterized by a rough topography composed of isolated volcanic edifices typically constructed on old (>20 Ma) and rigid oceanic lithosphere (Orellana-Rovirosa and Richards, 2017). In contrast, hotspot track ridges that form proximal to a spreading center (near-ridge setting) are generally characterized by smooth topography, with intrusive magmatism in the young (<10 Ma), weak oceanic lithosphere (Pollack et al., 1981; Orellana-Rovirosa and Richards, 2017; Contreras-Reyes et al., 2022).

Velocity-depth models obtained from wide-angle seismic data show how the structure of the crust and upper mantle is affected by hotspot magmatism (e.g., Richards et al., 2013). Examples of off-ridge hotspot trails such as the Juan Fernández Ridge (Kopp et al., 2004) and Hawaii (McGregor et al., 2023; Dunn et al., 2024) show a generally normal-thickness oceanic crust deformed (deflected) by the weight of the volcanic edifice (Manríquez et al., 2014; Watts et al., 2021; McGregor et al., 2023). In contrast, on-ridge hotspot trails such as the Cocos (Walther 2003), Carnegie (Sallares et al., 2003), and Nazca Ridges (Hampel et al., 2004; Contreras-Reyes et al., 2022) have an anomalously thick crust (>10 km) but a similar velocity-depth structure to that of standard oceanic crust (Christeson et al., 2019; Grevemeyer et al., 2018a; White et al., 1992). In addition, some off-ridge hotspot trails are characterized by oceanic crust that is highly intruded, with intrusions forming a dense, high P-wave velocity (>6.0 km/s) core; for example, the Great Meteor seamount (Weigel and Grevemeyer, 1999), Hawaii (McGregor et al., 2023; Dunn et al., 2024), Tenerife (Canales et al., 2000), and the Louisville Ridge (Contreras-Reyes et al., 2010; Robinson et al., 2018).

In this paper, we investigate the lithological structure of the Louisville Ridge (LR), which formed in an off-ridge setting more than 500 km away from a spreading center axis. Two-dimensional P-wave (V_p) velocity-depth models reveal that LR seamounts contain intrusive cores characterized by a $V_p \geq 6.0$ km/s (Contreras-Reyes et al., 2010; Stratford et al., 2015; Funnell et al., 2017; Robinson et al., 2018), in contrast to the adjoining Pacific oceanic crust which is unaffected by hotspot-related magmatic activity. Contreras-Reyes et al. (2010) interpreted these high V_p regions as comprising basaltic and intrusive rocks that form a symmetrical, semi-conical core, implying that the seamount has undergone growth both vertically and laterally. To gain further insight into the seismic structure of the 27.6°S seamount, and what its lithological implications are, we model the S-wave velocity (V_s) structure in the vicinity of the summit and surroundings areas. We derive both 2-D V_p and V_s tomographic inversion models along one wide-angle seismic profile that intersects the 27.6°S seamount and follows a sub-perpendicular trend across the LR (profile P03 shown in Fig. 1). The sediment thickness along-profile is constrained by a coincident multichannel seismic profile (Fig. 2). We further use these models to calculate a V_p/V_s ratio model, which provides valuable constraint for deciphering the lithological composition of the oceanic crust and upper mantle (Christensen 1996; Carlson & Miller, 2003; Grevemeyer et al., 2018b; Li et al., 2022; Contreras-Reyes et al., 2022, 2023).

Hotspot magmatism can also result in upper mantle anisotropy. Initially, seismic anisotropy is governed by the lattice preferred orientation (LPO) of olivine acquired during the formation of the oceanic lithosphere at mid-ocean ridges (Nicolas and Christensen, 1987). Compressional waves exhibit their highest speed (fast direction) along the *a*-axis of olivine, typically aligning with the direction of plate motion/mantle flow (Hess, 1964; Skemer and Hansen, 2016). However, some refraction experiments that have measured upper mantle P-wave velocity away from the spreading center indicate a rotation relative to a paleo spreading direction. This has been attributed to various processes, including mantle serpentinization induced by plate bending (Contreras-Reyes et al., 2008; Mishra and Gordon, 2016), the presence of 3-D mantle flow patterns instead of exclusively 2-D corner flow in the plate direction (VanderBeek et al., 2016; Toomey et al., 2007), upwelling of a hotspot mantle plume (Fontaine et al., 2005), and a complex configuration of cracks (Mark et al., 2019).

We present 2-D V_p and V_s models for the oceanic crust formed >90 Ma at the Osbourn Trough, an extinct spreading center (Worthington et al., 2006). Here, we also model lithospheric mantle refractions (P_n) with offsets of up to 150 km, generated with an active seismic source, which sample up to a depth of ~30 km below seafloor (*bsf*). We compare our results with previous, and orthogonal, 2-D V_p models obtained along the LR (Stratford et al., 2015; Funnell et al., 2017; Robinson et al., 2018) to further study the magnitude of seismic anisotropy within the uppermost 3-4 km of the mantle. Finally, we discuss our results in terms of hotspot magmatism and upper mantle seismic anisotropy.

2. Geological Setting

The Pacific Plate undergoes oblique subduction beneath the overriding Indo-Australian Plate with an approximate azimuth of N60ºW (e.g., Bird, 2003) and with a high convergence rate of ~240 mm/yr (DeMets et al., 2010; Seton et al., 2012). This, combined with the LR oblique alignment relative to the trench axis, results in the southward migration of the LR-trench intersection. Lonsdale (1988) and Balance et al. (1989) estimate the rate of southward migration to be 120-180 mm/yr. This migration leads to lateral variations in the structural composition of the trench (e.g., Clift et al., 1998), forearc (Clift and MacLeod, 1999; Contreras-Reyes et al., 2011), arc (England et al., 2004), and backarc (Bevis et al., 1995). In particular, the collision between the LR and the Indo-Australian Plate has accelerated subduction erosion, causing the arc-ward migration of the trench axis and the regional subsidence of the easternmost portion of the overriding plate (Ballance et al., 1989; Clift et al., 1998).

The LR marks a major hotspot track that stretches for over ~4,300 km, that was formed by the interplay between the Pacific Plate and the Louisville hotspot mantle plume located >500 km from the SW Pacific-Antarctic spreading center axis (Fig. 1A; Craig and Sandwell, 1988; Lonsdale, 1986; Downey et al., 2007). The LR comprises a succession of seamounts (Fig. 1C), with Osbourn being the oldest (prior to subduction) based on the dating of rock samples dredged along its length (Koppers et al., 2004, 2011). Along the Tonga-Kermadec Trench, the subducting old, cold Pacific Plate (>90 Ma) has a prominent outer rise-forebulge region, that is characterized by extensively fractured oceanic basement as a result of extensional bending-related faulting (Ballance et al., 1989; Contreras-Reyes et al., 2011; Stratford et al., 2015; Funnell et al., 2017; Robinson et al., 2018). At the point of LR-Tonga-Kermadec Trench collision, however, the trench-outer rise is further deformed by the significant elevation of Osbourn seamount; the next seamount to subduct (Ballance et al., 1989; Robinson et al., 2018). Here, the seafloor shallows by approximately 4,000-5,000 m (Fig. 1B).

The LR has volcanic edifices of 4,000-5,000 m in height (Fig. 1C) and is flanked by a flexural moat (Fig. 2) possibly filled by a mixture of volcaniclastic material, eroded island volcanic debris, and pelagic sediments. Contreras-Reyes et al. (2010) show a V_p of 4.0-4.5 km/s at depths of 1.0-1.5 *bsf* adjacent to the 27.6ºS seamount, consistent with volcaniclastic material as interpreted from the seismic models of Great Meteor seamount (Weigel and Grevemeyer, 1999), Marquesas (Caress et al., 1995; Wolfe et al., 1998), Tenerife (Watts et al., 1997), and Hawaii (Dunn et al., 2024). Most of the volcaniclastic material and eroded island volcanic debris that form part of the infill material were likely deposited during and/or a few years after seamount formation when the volcano was active (68-69 Ma). Subsequently, sedimentation is expected to be continuous, forming a thin pelagic drape (Fig. 2).

3. Seismic Data and Tomographic Inversion

3.1. Seismic data

Seismic profile P03 is located ~150 km to the east of the Tonga-Kermadec Trench axis (Fig. 1), crossing the LR axis obliquely and running through the 26.7ºS seamount. It is aligned sub-parallel to the trench axis, an orientation chosen to mitigate the structural inheritance of plate-bending in the outer rise region (Grevemeyer and Flueh, 2008). Both multichannel seismic (MCS) reflection and wide-angle (WA) seismic refraction data were acquired along profile P03.

For the MCS survey, a 100 m-long, 16-channel streamer was used for acquisition which aimed to image the top of the oceanic basement. Fig. 2 shows the sediment layer which includes a prominent intra-sediment reflector. This reflector is interpreted as an unconformity that records subsidence of the crust under seamount loading. For the WA survey, a total of 33 GEOMAR Ocean-Bottom Hydrophones/Seismographs (OBH/S) were deployed along the ~368 km profile, with a spacing of ~9 km between each instrument (Fig. 1). The seismic source, used for both WA and MCS contemporaneous acquisition, comprised two sub-arrays, each of six G airguns, which collectively had a total volume of 84 l. This source was fired every 60 s at a pressure of 3,000 psi. The WA seismic processing procedure included clock drift correction, location on seabed determination, band pass filtering at 1/4/40/50 Hz, and deconvolution. P-wave arrivals are observed to greater than 200 km receiver-shot distance. Example record sections are shown in Figs. 3-5, with observed phases annotated.

Most OBSs also record prominent P-to-S mode-converted phases (Fig. 6) with high signal-to-noise ratio adjacent to the 27.6ºS seamount, such as converted crustal refractions (PS_gP), Moho reflections (PS_mSP), and mantle refractions (PS_nP). Unfortunately, the PS_gP and PS_mSP phases beneath the 27.6ºS seamount (>2 km depth below the summit) are obscured by the P_g and P_mP phases, and the P-wave seabed-sea surface multiples.

3.2 V_p and V_s tomographic inversion approach

Tomographic models were obtained using the 2-D method developed by Korenaga et al. (2000). This approach enables the combined inversion of seismic reflection and refraction phases for a single two-dimensional layer. For modelling, the thickness of the water layer was determined from the swath bathymetry data, while the sediment layer thickness was determined by converting the two-way travel (TWT) time measurements of the corresponding reflectors in the MCS data into depth (Fig. 2). The time-to-depth conversion used a fixed velocity of 1700 m/s, the average P-wave velocity for pelagic sediment (Tenzer and Gladkikh, 2014). While lateral variations in this velocity might cause errors in the modelled P-S-P travel times, the range of sediment velocities expected (1.6-2.0 km/s; Hamilton, 1976; Fulthorpe et al., 1989; Tenzer and Gladkikh, 2014) around the Louisville Ridge results in a maximum error of 20 ms. This is well within the observed P-S-P phase picking error of 70-90 ms. Therefore, using a fixed velocity for depth determination is appropriate given th overall travel time pick error.

In the V_p inversion, we used the P_g picks and initial model of Contreras-Reyes et al. (2010). Here, we further incorporate P_n picks (>100 km receiver-shot offset; Figs. 3-5). Fig. 7A shows the resulting 2-D V_p inversion model in which the upper mantle is constrained to depths of ~30 km.

For the V_s inversion, we used the PSP phase picks, where that arrival is interpreted to originate at the interface between the sedimentary layer and crystalline basement away from the 27.6ºS seamount, and at the bottom of the pelagic sediment layer near the seamount (Figs. 2 and 6), where the acoustic impedance ($Z = \rho V$) contrast is most likely largest (Zoeppritz 1919; Trummer, 2002). The latter is supported by many other studies such as Au and Clowes (1984), Contreras-Reyes et al. (2008, 2022, 2023), Latta and Dunn (2020), Li et al. (2021), Grevemeyer et al. (2018b), Guo et al. (2023), Spudich and Orcutt (1980), Trummer (2002) and White and Stephen (1980); see reference seismic velocity and density values in Fig. 6. Near the seamount's flanks (where the moat-depression is filled by volcanoclastic material), the most likely seismic interface for P-to S-wave conversion is the volcanic clastic material/pelagic sediment interface (Fig.6).

Seismic studies conducted in settings where the oceanic crust has not been affected by hotspot magmatism (without a flexural moat filled with volcaniclastic material) show a relatively thin pelagic sediment layer (<500 m; Au and Clowes, 1984; Contreras-Reyes et al., 2008, 2022, 2023; Latta and Dunn, 2020; Grevemeyer et al., 2018b; Spudich and Orcutt, 1980; Trummer, 2002; White and Stephen, 1980 among others). For these studies, the high acoustic impedance contrast between pelagic sediment and oceanic igneous crust (Fig. 2A) at the sediment/oceanic crust interface promotes P-to-S-wave conversion.

Near the 27.6ºS seamount, the infill material within the flexural moat has a V_p of 4.0-4.5 km/s at depths of 1.0-1.5 *bsf* (Contreras-Reyes et al., 2010). These values are similar to those measured in the uppermost oceanic crust (Grevemeyer et al., 2018a; Christeson et al., 2019) and result in a weak velocity and density contrast at the infill material/basement interface. In contrast, pelagic carbonate sediments usually have V_p and density values of 1.6-2.0 km/s and 1,700 kg/m^3, respectively (Hamilton 1976; Fulthorpe et al., 1989; Tenzer and Gladkikh, 2014), which results in higher acoustic impedance contrasts at the pelagic sediment/infill material interface than at the infill material/basement interface (Fig. 6).

For the V_s inversion, we used converted P-S-P crustal phases with picking uncertainties smaller than 100 ms. Due to our conservative selection of converted S-waves arrivals for picking, the V_s model has lower spatial coverage than the V_p model. We applied damping constraints to maintain a consistent V_p within the pelagic sedimentary layer. The initial 2-D V_s model was constructed by dividing the final inverted 2-D V_p model by a constant V_p/V_s ratio of 1.8 (see Supporting Information (SI)). Thus, the V_s inversion is independent of the V_p inversion, but the initial V_s model is dependent on the final V_p model. Despite this limitation, the high-density of OBH/S receivers and shots used in controlled seismic source experiments (the case here), provides better resolution for crust and uppermost mantle than, for example, that provided by 3-D earthquake tomography.

V_s tomographic inversions all converge to a similar outcome, regardless of which V_p/V_s ratio in the range of 1.65 and 1.85 is used to construct the initial model. The final 2-D V_s and V_p/V_s models are presented in Figs. 7B and 7C, respectively. See Sections 3.3 and 3.4 and SI for details of the resolution and uncertainty of the V_p and V_s models.

3.3 Resolution of the V_p and V_s models

To assess the resolvability of the obtained velocity models, we constructed synthetic velocity models by applying Gaussian anomalies (Figs. 8A and 8B for V_p and V_s inversion, respectively) to the final inversion velocity models shown in Figs. 7A and 7B for V_p and V_s, respectively. Each anomaly has a maximum amplitude of ±5% in velocity. Synthetic travel time data with the same source-receiver geometry as the actual dataset, were generated using the perturbed models. Subsequently, these data were inverted using an initial unperturbed model, and the velocity anomalies recovered appraised. The results show that most of the velocity anomalies are reasonably well reproduced in position, shape, and amplitude. Some of the recovered velocity anomalies show certain shape deterioration in the upper mantle (Figs. 8C and 8D) and for the V_s inversion in particular at the NE edge of the model (Fig. 8D). Nevertheless, the results show that the geometry and instrument spacing provide sufficient resolution to discern most of the velocity anomalies, and are capable of distinguishing between positive and negative variations.

We also compute the Derivative Weight Sum (DWS), a proxy for the ray density (Korenaga et al., 2000), for the V_p and V_s models (Figs. 8E and 8F). Most of the oceanic crust and uppermost mantle have good coverage for the V_p model (except the edges of the models and the mantle at greater than 20 km depth). For the V_s model, DWS values are high to the NE of 27.6ºS seamount, but negligible beneath it.

3.4 Uncertainties in the V_p and V_s models

To assess the accuracy of the final model, we adopted a Monte Carlo approach (Korenaga et al., 2000) which consisted of randomly perturbing velocities in our reference model. Specifically, we generated 10 distinct initial velocity models by adding randomly distributed perturbations. For the P- and S-wave models, respectively. For the 2-D initial P-wave velocity models, we applied smooth perturbations distributed randomly, with maximum velocity perturbations reaching ±5% of the original amplitude. Additionally, we introduced phase errors (±50 ms) and common receiver errors (±50 ms) to the original dataset to establish corresponding perturbed travel times, following the approach outlined by Korenaga et al. (2000). A similar procedure was followed for the S-wave velocity model.

Subsequently, we conducted a tomographic inversion for each velocity model using a single noisy dataset. This allowed us to evaluate not only the solution's reliance on the reference model but also the impact of phase arrival time picking errors. The termination criterion for each inversion was set at $\chi^2 < 1$ (when the travel time fit becomes lower than the travel time uncertainties).

Figs. 8G and 8H show the calculated percentage standard deviation (ΔV) for the average velocity-depth model from the ten final models for both P- and S-wave velocity. The root-mean-square travel time misfit (T_{RMS}) and χ^2 parameter for the final model are summarized in the SI. The ΔV is generally lower than 0.2 km/s (≤4%) for both models with average values of 1.5%.

Figs. 9A and 9B show the calculated V_p/V_s model and its standard deviation $\Delta\left(\frac{V_p}{V_s}\right)$, computed as

$$(1) \quad \Delta\left(\frac{V_p}{V_s}\right) = \pm\left(\frac{V_p}{V_s}\right)\sqrt{\left(\frac{\Delta V_p}{V_p}\right)^2 + \left(\frac{\Delta V_s}{V_s}\right)^2}$$

where ΔV_p and ΔV_s correspond to the uncertainties of the V_p and V_s models, respectively. Overall, $\Delta\left(\frac{V_p}{V_s}\right)$ magnitudes are lower than 0.06 and reach maximum values of 0.1 in the summit region of the 27.5ºS seamount (Fig. 9B).

4. Results and Interpretation

We summarize the seismic findings in three contexts: (1) sediment/volcaniclastic deposits; (2) seismic structure of the Pacific crust and upper mantle adjacent to the 27.6ºS seamount (NE and SW domains along profile P03) unaffected by hotspot magmatism; and

(3) seismic structure of the crust beneath the 27.6ºS seamount that results from hotspot magmatism.

4.1. Sediment/volcaniclastic deposits layer

The sediment layer has a thickness of between 100 m at the NE and SW end of the profile to 1,200-1,500 m on the flanks adjacent to the 27.6°S seamount (Fig. 2). The P-wave velocity within this layer ranges from 1.6 km/s at the seabed to between 1.7 and 4.0-4.5 km/s at 5.5-6.0 km depth, depending on seamount proximity (Fig. 7). The P-wave model shows a moat-like depression around the seamount, up to 200 km across, and having a maximum depth of 1,000-1,500 m at 160 km and 240 km along-profile (Fig. 7). This moat is formed by the flexure of the oceanic lithosphere under the load of the LR, and the seismic velocity-depth structure suggests that its infill is composed mainly of volcaniclastic material (Contreras-Reyes et al., 2010; Watts et al., 2021; McGregor et al., 2023; Dunn et al., 2024; Xu et al., 2023).

The infill material within the flexural moat adjacent to the 27.6ºS seamount was interpreted as an accumulation of volcaniclastic and debris flow deposits based on the range in P-wave velocity of 1.9-4.0 km/s observed by Contreras-Reyes et al. (2010). A few hundred meters below seafloor, V_p ranges from 1.7 to 1.9 km/s in the vicinity of the seamount, indicating the likely presence of a pelagic drape, hyaloclastics, or sub-areal volcanic rocks (Grevemeyer and Flueh, 2008; Contreras-Reyes et al., 2010). The base of the pelagic sedimentary layer is highlighted by the intra-sediment reflector shown in Fig. 2. Specifically, around the moat a discontinuity likely separates pelagic sediment and eroded oceanic island material from volcaniclastic deposits formed during the creation of the 26.7ºS seamount. Our 2-D V_s inversion model reveals velocities within the volcaniclastic layer ranging from 1.8 to 2.8 km/s (Fig. 7B), which results in a V_p/V_s ratio of between 1.7-1.75, which is similar to that obtained by laboratory measurements of pillow basalts (Fig. 7B; Christensen, 1996; Carlson and Miller, 2003).

4.2 Seismic structure of the Pacific crust and upper mantle adjacent to the 27.6ºS seamount

To the NE and SW of 27.6ºS seamount, the Pacific upper crust (oceanic crustal seismic layer 2) is approximately 1.5-2.0 km thick and has a P-wave velocity ranging between 4.0 and ~6.7 km/s (Fig. 7A). The corresponding S-wave velocity ranges between 2.5 and 3.0 km/s and is similar to that of the volcaniclastic deposits sited in the deeper portion of the moat. The V_p/V_s ratio ranges between 1.7 and 1.8. At the upper-to-lower crust transition (boundary between seismic layer 2 and 3), V_p and V_s velocities are 6.4-6.7 km/s and 3.3-3.7 km/s, respectively, corresponding to a V_p/V_s ratio of 1.7-1.85. The V_p/V_s values observed at the top and bottom of the upper crust of ~1.7-1.85 are consistent with laboratory measurements of basalts and diabase reported by Christensen (1996) and Carlson and Miller (2003).

At a distance of more than 50 km to both the NE and SW from the 27.6ºS seamount, the lower crust (seismic layer 3) has a thickness of ~4 km within an overall crustal thickness of 5.5-6.0 km. Lowermost crustal P-wave velocities range between 7.0-7.2 km/s, whereas S-wave velocity ranges between 3.7-4.0 km/s, with corresponding V_p/V_s ratios of 1.7-1.85 (Figs. 7 and 9). These $V_p/V_{s.}$ values are slightly lower but still in agreement with laboratory measurement of gabbroic samples reported by Christensen (1996) and Carlson and Miller (2003).

The P-wave velocity within the uppermost mantle increases significantly from 8.1 to ~8.9 km/s from the seismic Moho to a depth of ~30 km, except to the SW, furthest from the Osbourn Trough. Here, the P-wave velocity varies from 8.1 to 8.4 km/s at equivalent depths. V_s ranges from 4.5 to 4.7 km/s, with a corresponding V_p/V_s ratio of 1.8-1.9 between 0 km and 300 km along-profile (Figs. 7, 10, 11). At the SW end of the profile, the V_p/V_s ratio is lower at 1.65-1.8, which we interpret as reflecting a region of dry mantle peridotite (e.g., Christensen, 1996). We attribute the region of relatively elevated V_p/V_s of 1.8-1.9 to reflect anhydrous mantle. This interpretation contrasts with studies that associate a V_p/V_s range of 1.8-1.9 with serpentinized mantle (e.g., Christensen, 1996; Carlson and Miller, 1997; 2003). This alternative interpretation will be discussed in Section 5.

4.3 Seismic structure of the crust beneath the 27.6ºS seamount

Near the summit of 27.6°S seamount, the P-wave model shows velocities in the range 6.0-6.5 km/s (Fig. 7A) overlying an apparent intrusive core (V_p = 6.5-7.5 km/s). Similar features are also observed at Osbourn and 28.5ºS seamounts (Robinson et al., 2018). The S-wave velocity-depth model exhibits velocities in the range 3.2-3.4 km/s in the near sub-seabed, resulting in a V_p/V_s ratio of 1.85-1.95 (Figs. 7B and 7C). Such V_p/V_s values are higher than those observed in the upper crust, particularly when compared to similar subseabed depths away from the seamount (Figs. 7-9). Such elevated V_p/V_s ratios are indicative of basaltic rocks with a high degree of porosity and fracturing (Christensen, 1996). Lower V_p/V_s ratios are observed adjacent to the seamount, which are interpreted as reflecting volcaniclastic and debris flow deposits (Fig. 9).

5. Discussion

5.1. Volcaniclastic and sediment deposition around the 27.6ºS seamount

Seamount formation induced by plate-hotspot interaction involves episodic eruptions and the deposition of volcaniclastic material. Consequently, significant clastic volumes amass in the summit and upper flanks. The susceptibility to mass wasting events and subsequent re-sedimentation in these regions contributes to the development of debris flows along the flanks and aprons (Moore et al., 1978; Wolfe et al., 1994). Furthermore, large-scale landslides and avalanches may occur, that can span hundreds of kilometers, as has been reported for Hawaii (Moore et al., 1978), La Reunion (Lenat et al., 1978), Tenerife (Watts and Masson, 1984), Great Meteor (Weigel and Grevemeyer, 1999), and Marquesas (Wolfe et al., 1994).

Following the passage of the Pacific Plate over the LR hotspot mantle plume, volcaniclastic deposition ceases, and sedimentation is primarily attributed to pelagic deposition and sub-aerial island erosion. According to 40Ar/39Ar age progression along the Louisville seamount trail (Koppers et al., 2004, 2011), the 27.6ºS seamount was active some 68-69 Ma, with a plate age of ~20 Myr at that time (Mueller et al., 2008). Pelagic sediment accumulates at remarkably slow rates of 2-10 m/Myr (Straume et al., 2019; Rotzien et al., 2022), which would result in a pelagic sediment thickness of 130-700 m in our study area. This thickness range is consistent with our observations from the MCS data away from the seamount regions (between 100 km and 300 km along-profile distance; Fig. 2). On the flanks of the seamount, the material lying above the volcaniclastic deposits is most likely to be a mixture of sub-aerial erosion products and pelagic drape.

We interpret the velocity-depth structure (V_p = 2.0-4.0 km/s, V_s = 1.8-2.4 km/s and V_p/V_s = 1.7-1.8; Fig. 7) observed above the oceanic basement as a mixture of volcaniclastic deposits such as breccias, tephra, slump blocks, and lava flows (Staudigel and Schmincke, 1983). Weigel and Grevemeyer (1999) note that these deposits exhibit a significantly higher porosity when compared to basaltic lavas extruded during crustal accretion at deeper water spreading centers. Our model shows a P-wave velocity greater than 4.0 km/s in the uppermost oceanic crust adjacent to the LR (*i.e.* unaffected by hotspot magmatism; Fig. 7), indicating a porosity lower than the volcaniclastic deposits. The upper crust, with a thickness of 1.0-1.5 km (see Section 3.2), has a velocity-depth structure characteristic of pillow lavas overlying a sheeted dike complex (Vera et al., 1990; Carlson, 2001; Christeson et al., 2019).

At the summit of the 27.6ºS seamount, the upper part exhibits a layer characterized by a P-wave velocity in the range 4.5-6.0 km/s and thickness of <1.0 km. This layer undergoes a transition to higher velocities (>6.4 km/s; Figs 7 and 10) consistent with the contact between alkali basaltic pillow lavas and intrusive rocks. However, the V_p/V_s ratio range of 1.85-1.95 in this region is remarkably higher than those observed at the flanks of the 27.6ºS seamount (V_p/V_s = 1.7-1.8; Figs. 7 and 9) but is also observed in laboratory measurements of pillow basalts and diabase complexes (Fig. 9; Christensen, 1996). This suggests, in the summit region, the presence of pillow basalts and intrusive rocks characterized by water-saturated cracks and fractures (Popp and Kern, 1994; Wang et al., 2012). These geological features are likely the result of eruptions taking place at shallower depth (Peterson and Moore, 1976).

Most likely, the now shallow crustal depth of the intrusive core in the summit region results from many tens of millions of years of erosion. Although converted P-S-P-waves are confined to depths of 1-2 km beneath the top of the seamount, these seismic phases are prominent (see Fig. 5) and constrain (to a limited depth) the relatively high V_p/V_s ratio beneath the summit.

5.2. Intrusion beneath the 27.6ºS seamount

Unfortunately, the V_s model does not constrain the middle and lower crustal sections of the 27.6ºS seamount due to the lack of recorded mode-converted S-waves that would have propagated within the volcanic edifice (Fig. 7). Nevertheless, the P-wave model reveals a region of high velocity (6.5-7.5 km/s) that can be interpreted as a symmetrical, semi-conical-shaped core (Fig. 7; Contreras-Reyes et al., 2010). Similar observations have been reported for Great Meteor seamount (Weigel and Grevemeyer, 1999), and the volcanic oceanic islands of Hawaii (Zucca et al., 1982; McGregor et al., 2023; Dunn et al., 2024) and Tenerife (Canales et al., 2000). Conversely, other seamounts exhibit a conical structure with lower relative P-wave velocity (<5.5 km/s), which has been interpreted to reflect construction by extrusive processes. Some examples include the Juan Fernández Ridge (Kopp et al., 2004), Musicians Seamount Province (Kopp et al., 2003), Jasper seamount (Hammer et al., 1994), and the Marquesas islands (Caress et al., 1995).

Along the LR, Robinson et al. (2018) also report the presence of discrete cores of high V_p (≥6.0 km/s) for the Osbourn and 28.5ºS seamounts (Figs. 1 and 11). In each case, the high V_p (≥6.0 km/s) region extends upwards to depths of 1.0-1.5 km beneath each summit. Canopus seamount (the widest) is similarly interpreted to have a predominantly intrusive composition, albeit the higher velocity core only extends upward to 2.0-3.0 km beneath its summit (Robinson et al., 2018).

Within the lowermost crust beneath 27.6ºS seamount, P-wave velocities exceed 7.2-7.5 km/s (Fig. 7), lying in the range observed for gabbroic (6.9-7.2 km/s) and peridotite/dunite (7.9-8.1 km/s) lithologies, as determined in laboratory experiments (e.g., Carlson and Miller, 2003; Christensen, 1996). Similar values are observed in seismic experiments for the lower crust and upper mantle, respectively (Grevemeyer et al., 2018a; Christeson et al., 2019). Contreras-Reyes et al. (2010) and Richards et al. (2013) have interpreted the high P-wave velocity regions in the lower crust beneath the LR to result from the intrusion of relatively buoyant intrusive bodies at just above Moho depth within the crust, in contrast to findings at the Marquesas (Caress et al., 1995) and Reunion (Charvis et al., 1999) islands, where such bodies are located beneath the Moho.

5.3. Upper mantle structure

Our seismic results reveal a notably elevated V_p, ranging from ~8.1 to ~8.9 km/s, within the uppermost ~15 km of the oceanic mantle in the NE segment and beneath the 27.6ºS seamount of profile P03 (Fig. 7). Towards the SW, there is a localized reduction in the upper mantle P-wave velocity, ranging from 8.1 to 8.3 km/s, such that the upper mantle velocity-depth structure appears asymmetric about 27.6ºS seamount (even considering the maximum V_p uncertainty of 0.2 km/s; Fig. 8G). There is also no evidence to support the presence of sub-crustal bodies/magmatic underplating centered beneath the LR at this location, equivalent to that reported by Watts et al. (1985), Caress et al. (1995), and Charvis et al. (1999) beneath the Hawaiian, Marquesas, and Reunion islands, respectively.

In the NE segment, where a $V_p \geq 8.0$ km/s and $V_s \geq 4.5$ km/s are observed, there is a notable region characterized by relatively high V_p/V_s ratios of 1.8-1.9. These ratios exhibit a decreasing trend to 1.7-1.8, predominantly in the SW sector of the seamount, at depths of 1-3 km below the Moho (Figs. 7 and 9). V_p/V_s ratios higher than 1.8 are usually interpreted in terms of some degree of hydration of the mantle. For example, Carlson and Miller (2003) estimated that V_p and V_s values of ~7.7 and ~3.9 km/s ($V_p/V_s \sim 1.97$) reflect a serpentine content of 20% (by volume) or 3% H_2O (by wt%). In the context of their linear relationship, the endmember composition of dry mantle peridotite is attained with V_p and V_s values of ~8.1 and ~4.3 km/s (V_p/V_s ~1.88). These values are somewhat higher when compared to Christensen (1996) who reported V_p/V_s of ~1.75 for mantle dunite at 200 MPa.

Contreras-Reyes et al. (2008) interpreted V_p/V_s ratios exceeding 1.8 as indicative of partial hydration resulting from bending-related faulting off southern Chile. This faulting has the potential to breach the entire oceanic crust, establishing pathways for water migration to upper mantle depths (Kopp et al., 2004; Contreras-Reyes et al., 2008; Grevemeyer et al., 2018). The down-going Pacific Plate adjacent to the Tonga-Kermadec Trench has well-developed bending-related faulting as shown by bathymetric maps, seismic reflection data (Funnell et al., 2014, 2017) and low upper mantle velocities (7.4-7.9 km/s) in the trench-outer rise region (Contreras-Reyes et al., 2011; Stratford et al., 2015; Funnell et al., 2017; Robinson et al., 2018; Fig. 1). However, strong plate bending stresses prior to plate subduction are confined to near the trench-outer rise region, where the plate curvature is higher. In contrast, bending-related faulting becomes weaker or absent away from the trench axis (typically >120 km seaward of the trench axis; Contreras-Reyes and Osses, 2010; Watts and Hunter, 2016).

The NE segment of profile P03 lies ~150 km from the trench axis (Fig. 1). Notably, the 2-D V_p model does not show evidence of reduced velocity in the crust or in the upper mantle (Fig. 7) relative to what might be expected for normal oceanic crust and mantle (e.g., Grevemeyer et al., 2018a). This observation implies that the seismic structure of the upper oceanic lithosphere remains unaffected by plate bending in this region. Hence, the elevated V_p/V_s ratio of 1.8-1.9 in the upper mantle is likely due to other factors.

The SW segment of profile P03 is located ~100 km from the trench axis, (Fig. 1). In this region, the 2-D V_p model does not show any evidence of reduced velocity in the crust, but the upper mantle exhibits a distinct zone of reduced P-wave velocity compared to the NE portion (Fig. 7). Nevertheless, the asymmetrical variation in upper mantle velocity along P03 may result from a complex interplay of processes, including mantle plume/lithosphere magmatic interaction, plate-bending related faulting, and the high anisotropy of mantle olivine. In this paper we investigate the likelihood of mantle anisotropy being the cause, by comparing our results with Robinson et al.'s (2018) P-wave model of profile PC which runs along the LR axis.

5.4. Upper mantle anisotropy of the Pacific Plate

Geophysical evidence supporting upper mantle anisotropy includes seismic tomography (Dunn et al., 2000), shear wave splitting (Russo et al., 2010), surface wave (Rayleigh and Love waves) dispersion (Regan and Anderson, 1984; Eddy et al., 2022), receiver function studies (Levin et al., 2002; Hu et al., 2015), and attenuation anisotropy (Nishimura and Forsyth, 1989; Becker and Lebedev, 2021). Generally, the two primary mechanisms invoked for the generation of upper mantle seismic anisotropy are Lattice Preferred Orientation (LPO) and directional mantle flow (Hess 1964; Zhang and Karato, 1995; Mark et al. 2019). Additionally, shape preferred orientation (SPO; Kern et al., 2008), partial melt and fluid alignment (Waff and Faul, 1992), and chemical variations (Khan et al., 2009) are also thought to be significant contributors to seismic anisotropy.

As olivine establishes a preferred orientation direction during flow or viscous shear deformation, it is not unreasonable to suppose that the P_n velocity perpendicular to the spreading center axis will be faster than spreading direction-parallel (Hess, 1964; Skemer and Hansen, 2016). For example, Mark et al. (2019) estimated a seismic anisotropy of 6.0 ± 0.3% at the Moho within 70 Ma lithosphere in the central Pacific. In addition, Shearer and Orcutt (1985) and Dunn et al. (2000) measured P_n anisotropy of 5.5% and 6-7% in the NW Pacific and at the East Pacific Rise, respectively, aligned parallel to the spreading direction. In contrast, 3-4% (Gaherty et al., 2004) or neglectable (de Melo et al., 2021) P_n anisotropy has been observed in the north and equatorial Atlantic, respectively, aligned parallel to the spreading direction. The reduced P_n anisotropy observed in the Atlantic implies increased conductive cooling at the corresponding portion of the Mid-Atlantic Ridge when the lithosphere formed and, consequently, increased localized (brittle) deformation within the mantle lithosphere and a limited extent of viscous deformation (Sleep, 1975; Gaherty et al., 2004).

Figs. 11A-11D show a comparison of the upper mantle P-wave structure between profiles P03 and PC (Robinson et al., 2018) in the proximity of the 27.6ºS seamount. To assess seismic anisotropy in this area, we utilize the anisotropic percentage, defined as

$$(2) \quad Anisotropic\ percentage = \frac{(V_f - V_s)}{V_f} \times 100\ (\%)$$

where V_f and V_s represent the faster and slower seismic velocities, respectively.

Mantle velocities modelled along profile P03 are faster than those along the southern portion of PC, except at the Moho (Fig. 11C) and we use these to calculate the minimum and maximum seismic anisotropic percentage, as shown in Fig. 11D. In both instances, P_n anisotropy increases with depth, reaching a maximum of ~6% at about 4 km depth beneath the Moho. The increase in P_n anisotropy with depth has also been measured by Mark et al. (2019), who reported a vertical velocity gradient of ~0.02 s^{-1} in the fast direction and 0 s^{-1} in the slow direction.

Our study area lacks a seismic profile oriented perfectly along the paleo spreading direction, as such, the upper mantle velocity is unconstrained in that direction. Nevertheless, we can extrapolate our results by noting that the azimuth (φ) between profile P03 and the paleo spreading direction is ~20º (φ_1), while that for profile PC is ~50º (φ_2) (Fig. 10A). We use a simplified expression to extrapolate the mantle P-wave velocity, V, as a function of the azimuth φ (in map view) in the form:

$$(3) \quad V(\varphi) = V_{max} - (V_{max} - V_{min})|\sin(\varphi)|$$

Here, we have assumed that the maximum velocity (V_{max}) is attained along the paleo spreading direction, while the minimum velocity (V_{min}) is perpendicular to this. This assumption is consistent with findings in the central Pacific (Hess, 1964; Mark et al., 2019). Thus, V_{max} and V_{min} can be written as:

$$(4) \quad V_{max} = V_1 - \left(\frac{V_1 - V_2}{|\sin(\varphi_1)| - |\sin(\varphi_2)|}\right)|\sin(\varphi_1)| \quad \text{and}$$

$$(5)\quad V_{min} = V_1 + \left(\frac{V_1 - V_2}{|\sin(\varphi_1)| - |\sin(\varphi_2)|}\right)[1 - |\sin(\varphi_1)|]$$

Here, V_1 and V_2 denote the upper mantle seismic velocities at the intersection of measured seismic profiles *1* and *2*, respectively, and it is assumed that $\varphi_1 \neq \varphi_2$. For example, Figs. 11E and 11F illustrate in polar coordinates the minimum and maximum values for V_1(P03) and V_2 (PC) at a specific depth, corresponding to azimuths of φ_1~20º and φ_2~50º, respectively. Thus, V_{max} and V_{min} are computed from Eqs. 4 and 5, enabling the determination of the semi-axes of the ellipses presented in Figs. 11E and 11F.

The comparison of upper mantle V_p between profiles P03 and PC reveals an increase in seismic anisotropy with depth within the uppermost 3-4 km of the mantle. The gradient of anisotropic percentage ranges between ~0.2 and ~2%/km (Figs. 11C and 11D), which is notably higher than that reported by Mark et al. (2019) in the central Pacific. Despite the simplicity of our P_n anisotropy estimation in the vicinity of the P03/PC intersection, which lacks azimuthal constraints, the resolution achieved by our active seismic study enhances the confidence in measuring a relatively high-velocity zone extending up to ~15 km below the Moho along P03.

6. Summary

A re-examination of wide-angle and reflection seismic data along a profile sub-perpendicular to the Louisville Ridge axis has revealed significant variations in P- and S-wave velocity when compared to typical oceanic crust at equivalent sub-basement depths. Adjacent to the 27.6ºS seamount, our results indicate a V_p/V_s ratio ranging from 1.7 to 1.8 in both the upper and lower oceanic crust, unaffected by hotspot magmatism. These results are consistent with documented V_p/V_s ratios obtained from laboratory measurements of gabbro and diabase. Conversely, in the vicinity of the seamount summit, there is a relatively higher V_p/V_s (~1.9), that is attributed to intrusive cores. At depths >1 km beneath the summit of the 27.6ºS seamount, our results suggest a predominance of intrusive features with a V_p ranging from 6.5 to 7.5 km/s.

V_p and V_p/V_s values of 2.0-4.0 km/s and 1.7-1.8, respectively, observed between the pelagic sediment layer and oceanic crust, indicate the possible presence of debris flows and eroded extrusive lavas. Notably, in the summit region, V_p (>6.0 km/s) and V_p/V_s (1.85-1.95) are remarkably higher than those observed in adjacent the upper oceanic crust (V_p = 4.0-6.0 km/s and V_p/V_s =1.7-1.8) at equivalent sub-basement depths. The observed relatively high V_p in the summit region reflects an intrusive core, extending upwards almost to the seafloor.

The average V_p/V_s ratio in the upper mantle NE of 27.6ºS seamount lies within the range of 1.8 to 1.9. To the SE of the seamount, there is a decrease in V_p/V_s ratio to 1.7-1.8 within the uppermost 4-5 km of the upper mantle. Additionally, an elevated V_p (~8.9 km/s) is observed at depths of 10-15 km below the Moho, both beneath the seamount and to the SW of it. In conjunction with a V_p model obtained along the Louisville Ridge axis (Robinson et al., 2018), our results indicate seismic upper mantle anisotropy of up to 6% at ~4 km below the Moho. Specifically, the fast axis is rotated by approximately 20º relative to the direction of the paleo spreading flow associated with the Osbourn Trough.

7. Acknowledgments

We thank the *Agencia Nacional de Investigación y Desarrollo* (ANID) for their support through FONDECYT grant 1210101. Seismic data acquisition during RV SONNE cruise SO195 was funded by the German Ministry of Education and Research (BMBF), grant 03G0195A. For the purposes of open access, the authors have applied a Creative Commons Attribution (CC-BY) license to any author accepted manuscript arising from this work. Finally, we thank the two anonymous reviewers whose comments improved the clarity of this paper.

References

Au, D., and Clowes, R. M. (1984). Shear-wave velocity structure of the oceanic lithosphere from ocean bottom seismometer studies. *Geophys. J. Int.*, *77*(1), 105–123. https://doi.org/10.1111/j.1365-246X.1984.tb01927.x

Ballance, P.F., Scholl, D.W., Vallier, T.L., Stevenson, A.J., Ryan, H. and Herzer, R.H., (1989), Subduction of a late cretaceous seamount of the louisville ridge at the tonga trench: a model of normal and accelerated tectonic erosion, *Tectonics,* 8(5), 953–962.

Bassett, D., Kopp, H., Sutherland, R., Henrys, S., Watts, A. B., Timm, C., ... and de Ronde, C. E. (2016), Crustal structure of the Kermadec arc from MANGO seismic refraction profiles. *J. Geophys. Res.: Solid Earth*, *121*(10), 7514-7546.

Becker, T. W., and Lebedev, S. (2021). Dynamics of the upper mantle in light of seismic anisotropy. *Mantle convection and surface expressions*, 257-282.

Bevis, M., Taylor, F.W., Schutz, B.E., Recy, J., Isacks, B.L., Helu, S., Singh, R., Kendrick, E., Stowell, J., Taylor, B. and Calmant, S., (1995), Geodetic observations of very rapid convergence and back-arc extension at the Tonga arc, *Nature,* 374**,** 249–251.

Bird, P. (2003), An updated digital model of plate boundaries. *Geochemistry, Geophysics, Geosystems*, *4*(3).

Canales, J. P., Dañobeitia, J. J., and Watts, A. B. (2000), Wide-angle seismic constraints on the internal structure of Tenerife, Canary Islands. *Journal of volcanology and geothermal research*, *103*(1-4), 65-81.

Caress, D. W., McNutt, M. K., Detrick, R. S., and Mutter, J. C. (1995). Seismic imaging of hotspot-related crustal underplating beneath the Marquesas Islands. *Nature*, *373*(6515), 600-603.

Carlson, R. L., and Miller, D. J. (2003). Mantle wedge water contents estimated from seismic velocities in partially serpentinized peridotites. *Geophys. Res. Lett.*, *30*(5).

Charvis, P., Laesanpura, A., Gallart, J., Hirn, A., Lépine, J. C., de Voogd, B., ... and Pontoise, B. (1999). Spatial distribution of hotspot material added to the lithosphere under La Réunion, from wide-angle seismic data. *J. Geophys. Res: Solid Earth*, *104*(B2), 2875-2893.

Christensen, N. I. (1996). Poisson's ratio and crustal seismology. *J. Geophys. Res*, 101(B2), 3,139-3,156. doi/10.1029/95JB03446

Christeson, G. L., Goff, J. A., and Reece, R. S. (2019). Synthesis of oceanic crustal structure from two-dimensional seismic profiles. *Reviews of Geophysics*, *57*(2), 504–529. https://doi.org/10.1029/2019rg000641

Clift, P.D., MacLeod, C.J., Tappin, D.R., Wright, D.J. and Bloomer, S.H., 1998. Tectonic controls on sedimentation and diagenesis in the Tonga Trench and forearc, southwest Pacific, *Bull. geol. Soc. Am.,* **110**(4), 483–496.

Clift, P.D. and MacLeod, C.J., 1999. Slow rates of subduction erosion estimated from subsidence and tilting of the Tonga forearc, *Geology,* **27**(5), 411– 414.

Contreras-Reyes, E., Grevemeyer, I., Flueh, E. R., Scherwath, M., and Bialas, J. (2008). Effect of trench-outer rise bending-related faulting on seismic Poisson's ratio and mantle anisotropy: A case study offshore of southern Central Chile. *Geophys. J. Int*, 173(1), 142-156.

Contreras-Reyes, E., Obando-Orrego, S., Cortés-Rivas, V., and Krabbenhoeft, A. (2022). Poisson’s ratio structure beneath the Nazca Ridge. *Geophysical Research Letters*, 49(9)

Contreras-Reyes, E., Obando-Orrego, S., and Grevemeyer, I. (2023), 2-D V_p and V_s Models of the Indian Oceanic Crust Adjacent to the NinetyEast Ridge. *Journal of Geophysical Research: Solid Earth*, *128*(3), e2022JB025701.

Contreras-Reyes, E., Grevemeyer, I., Watts, A. B., Planert, L., Flueh, E. R., and Peirce, C. (2010), Crustal intrusion beneath the Louisville hotspot track. *Earth and Planetary Science Letters*, *289*(3-4), 323-333.

Contreras-Reyes, E., and Osses, A. (2010). Lithospheric flexure modelling seaward of the Chile trench: implications for oceanic plate weakening in the Trench Outer Rise region. *Geophys. J. Int.*, *182*(1), 97-112.

Contreras-Reyes, E., Grevemeyer, I., Watts, A. B., Flueh, E. R., Peirce, C., Moeller, S., and Papenberg, C. (2011), Deep seismic structure of the Tonga subduction zone: Implications for mantle hydration, tectonic erosion, and arc magmatism. *J. Geophys. Res.: Solid Earth*, *116*(B10).

de Melo, G. W., Parnell-Turner, R., Dziak, R. P., Smith, D. K., Maia, M., do Nascimento, A. F., and Royer, J. Y. (2021). Uppermost mantle velocity beneath the Mid-Atlantic Ridge and transform faults in the Equatorial Atlantic Ocean. *Bulletin of the Seismological Society of America*, *111*(2), 1067-1079.

DeMets, C., Gordon, R.G. and Argus, D.F., 2010. Geologically current plate motions, *Geophys. J. Int.,* **181,** 1–80.

Deng, X., Luo, C., Wentzcovitch, R. M., Abers, G. A., and Wu, Z. (2022). Elastic anisotropy of lizardite at subduction zone conditions. *Geophys. Res. Lett.*, *49*(18), e2022GL099712.

Downey, N. J., Stock, J. M., Clayton, R. W., and Cande, S. C. (2007). History of the Cretaceous Osbourn spreading center. *J. Geophys. Res.: Solid Earth*, *112*(B4).

Dunn, R. A., Toomey, D. R., and Solomon, S. C. (2000). Three-dimensional seismic structure and physical properties of the crust and shallow mantle beneath the East Pacific Rise at 9 deg 30 min N. *J. Geophys. Res.*, *105*, 23.

Dunn, R. A., Watts, A. B., Xu, C., and Shillington, D. J. (2024), A seismic tomography, gravity, and flexure study of the crust and upper mantle structure across the Hawaiian Ridge: 2. Ka'ena. *Journal of Geophysical Research: Solid Earth*, *129*(2), e2023JB028118.

Eddy, C. L., Ekström, G., and Nettles, M. (2022), Three-dimensional seismic anisotropy in the Pacific upper mantle from inversion of a surface-wave dispersion data set. *Geophys. J. Int.*, *231*(1), 355-383.

England, P., Engdahl, R. and Thatcher, W., (2004), Systematic variation in the depths of slabs beneath arc volcanoes, *Geophys. J Int.,* 156(2), 377–408.

Fontaine, F. R., E. E. E. Hooft, P. G. Burkett, D. R. Toomey, S. C. Solomon, and P. G. Silver (2005), Shear-wave splitting beneath the Galápagos archipelago, *Geophys. Res. Lett*.,32, L21308, doi:10.1029/2005GL024014.

Fulthorpe, C. S., Schlanger, S. O., and Jarrard, R. D. (1989), In situ acoustic properties of pelagic carbonate sediments on the Ontong Java Plateau. *J. Geophys. Res: Solid Earth*, *94*(B4), 4025-4032.

Funnell, M. J., Peirce, C., and Robinson, A. H. (2017). Structural variability of the Tonga-Kermadec forearc characterized using robustly constrained geophysical data. *Geophys. J. Int*, *210*(3), 1681-1702.

Funnell, M. J., Peirce, C., Stratford, W. R., Paulatto, M., Watts, A. B., and Grevemeyer, I. (2014). Structure and deformation of the Kermadec forearc in response to subduction of the Pacific oceanic plate. *Geophys. J. Int*, *199*(2), 1286-1302.

Gaherty, J. B., D. Lizarralde, J. Collins, G. Hirth, and S. Kim (2004). Mantle deformation during slow seafloor spreading constrained by observations of seismic anisotropy in the western Atlantic, *Earth Planet. Sci. Lett*. 228, 255–265.

Grevemeyer, I., and Flueh, E. R. (2008), FS Sonne/Fahrtbericht/Cruise Report SO195: TOTAL TOnga Thrust earthquake Asperity at Louisville Ridge, Suva/Fiji-Suva/Fiji 07.01.-16.02. 2008.

Grevemeyer, I., Ranero, C. R., and Ivandic, M. (2018a), Structure of oceanic crust and serpentinization at subduction trenches. *Geosphere*, *14*(2), 395–418. https://doi.org/10.1130/ges01537.1

Grevemeyer, I., Hayman, N. W., Peirce, C., Schwardt, M., Van Avendonk, H. J. A., Dannowski, A., and Papenberg, C. (2018b), Episodic magmatism and serpentinized mantle exhumation at an ultraslow-spreading centre. *Nat. Geosc.*, *11*(6), 444–448. https://doi.org/10.1038/ s41561-018-0124-6

Hamilton, E. L. (1976). Variations of density and porosity with depth in deep-sea sediments. *J. Sedimentary Res.*, *46*(2), 280-300.

Hampel, A., Kukowski, N., Bialas, J., Huebscher, C., & Heinbockel, R. (2004). Ridge subduction at an erosive margin: The collision zone of the Nazca Ridge in southern Peru. *Journal of Geophysical Research: Solid Earth*, *109*(B2).

Hammer, P. T., Dorman, L. M., Hildebrand, J. A., and Cornuelle, B. D. (1994). Jasper Seamount structure: Seafloor seismic refraction tomography. *J. Geophys. Res.: Solid Earth*, *99*(B4), 6731-6752.

Hatakeyama, K., Katayama, I., Hirauchi, K. I., and Michibayashi, K. (2017), Mantle hydration along outer-rise faults inferred from serpentinite permeability. *Scientific Reports*, *7*(1),13870.

Hess, H. H. (1964). Seismic anisotropy of the uppermost mantle under oceans, *Nature*, *203*(4945), 629-631.

Hu, J., Yang, H., Li, G., and Peng, H. (2015), A review on the analysis of the crustal and upper mantle structure using receiver functions. *Journal of Asian Earth Sciences*, *111*, 589-603.

Hunter, J., and Watts, A. B. (2016), Gravity anomalies, flexure and mantle rheology seaward of circum-Pacific trenches. *Geophys. J. Int.*, *207*(1), 288-316.

Khan, A., Boschi, L., and Connolly, J. A. D. (2009). On mantle chemical and thermal heterogeneities and anisotropy as mapped by inversion of global surface wave data. *J. Geophys. Res.: Solid Earth*, *114*(B9).

Kern, H., Ivankina, T. I., Nikitin, A. N., Lokajíček, T., & Pros, Z. (2008). The effect of oriented microcracks and crystallographic and shape preferred orientation on bulk elastic anisotropy of a foliated biotite gneiss from Outokumpu. *Tectonophysics*, *457*(3-4), 143-149.

Koppers, A. A., Duncan, R. A., and Steinberger, B. (2004). Implications of a nonlinear 40Ar/39Ar age progression along the Louisville seamount trail for models of fixed and moving hot spots. *Geochemistry, Geophysics, Geosystems*, *5*(6).

Koppers, A. A., Gowen, M. D., Colwell, L. E., Gee, J. S., Lonsdale, P. F., Mahoney, J. J., & Duncan, R. A. (2011). New 40Ar/39Ar age progression for the Louisville hot spot trail and implications for inter–hot spot motion. *Geochemistry, Geophysics, Geosystems*, *12*(12).

Kopp, H., Kopp, C., Phipps Morgan, J., Flueh, E. R., Weinrebe, W., and Morgan, W. J. (2003). Fossil hot spot-ridge interaction in the Musicians Seamount Province: Geophysical investigations of hot spot volcanism at volcanic elongated ridges. *J. Geophys. Res.: Solid Earth*, *108*(B3).

Kopp, H., Flueh, E. R., Papenberg, C., and Klaeschen, D. (2004). Seismic investigations of the O'Higgins Seamount Group and Juan Fernández Ridge: Aseismic ridge emplacement and lithosphere hydration. *Tectonics*, *23*(2).

Lata, C., and Dunn, R. A. (2020). Uppermost crustal structure across the eastern Lau spreading center from P-to-S converted waves. *Marine Geophysical Research*, *41*(4), 20.

Li, Y., Grevemeyer, I., Huang, H., Qiu, X., and Xu, Z. (2021). Seismic constraint from V_p/V_s Ratios on the structure and composition across the continent-ocean transition zone, south China Sea. *Geophys. Res. Lett.*, *48*(16), e2021GL094656. https://doi. org/10.1029/2021gl094656

Levin, V., Park, J., Brandon, M., Lees, J., Peyton, V., Gordeev, E., & Ozerov, A. (2002), Crust and upper mantle of Kamchatka from teleseismic receiver functions. *Tectonophysics*, *358*(1-4), 233-265.

Lonsdale, P.F., (1986), A multibeam reconnaissance of the Tonga trench axis and its intersection with the Louisville guyot chain, *Mar. Geophys. Res.,* 8, 295–327.

Lonsdale, P., (1988), Geography and history of the Louisville Hotspot Chain in the southwest Pacific, *J. Geophys. Res.,* 93(B4), 3078–3104.

Manríquez, P., Contreras-Reyes, E., & Osses, A. (2014). Lithospheric 3-D flexure modelling of the oceanic plate seaward of the trench using variable elastic thickness. *Geophysical Journal International*, *196*(2), 681-693.

Mark, H. F., Lizarralde, D., Collins, J. A., Miller, N. C., Hirth, G., Gaherty, J. B., and Evans, R. L. (2019), Azimuthal seismic anisotropy of 70-Ma Pacific-plate upper mantle. *Journal of Geophysical Research: Solid Earth*, *124*(2), 1889-1909.

Masson, D. G. (1991), Fault patterns at outer trench walls, *Mar. Geophys. Res.*, 13, 209–225, doi:10.1007/BF00369150.

McGregor, B. G., Dunn, R. A., Watts, A. B., Xu, C., & Shillington, D. J. (2023). A seismic tomography, gravity, and flexure study of the crust and upper mantle structure of the Hawaiian Ridge: 1. *J. Geophys. Res.: Solid Earth*, *128*(12), e2023JB027218.

Mishra, J. K., and Gordon, R. G. (2016). The rigid-plate and shrinking-plate hypotheses: Implications for the azimuths of transform faults. *Tectonics*, 35, 1827–1842. https://doi.org/10.1002/2015TC003968

Mueller, R. D., Sdrolias, M., Gaina, C., and Roest, W. R. (2008). Age, spreading rates, and spreading asymmetry of the world's ocean crust: *G-Cubed* 9. *Q04006.*

Nicolas, A. & Christensen, N., (1987), *Composition, Structure and Dynamics of the Lithosphere-Asthenosphere System* eds Fuchs, K. and Froidevaux, C., pp. 111–123, Am. Geophys. Union, Washington, DC.

Nishimura, C. E., & Forsyth, D. W. (1989). The anisotropic structure of the upper mantle in the Pacific. *Geophys. J. Int. 96*(2), 203-229.

Orellana-Rovirosa, F., & Richards, M. (2017). Rough versus smooth topography along oceanic hotspot tracks: Observations and scaling analysis. *Geophysical Research Letters*, *44*(9), 4074-4081

Park, J., and Levin, V. (2002). Seismic anisotropy: tracing plate dynamics in the mantle. *Science*, *296*(5567), 485-489.

Peacock, S. M. (1993). Large-scale hydration of the lithosphere above subducting slabs. *Chemical Geology*, *108*(1-4), 49-59.

Pollack, H.N., Gass, I.G., Thorpe, R.S., Chapman, D.S., (1981), On the Vulnerability of Lithospheric Plates to Mid-Plate Volcanism: reply to comments by P.R. Vogt. *J. Geophys. Res*. 86 (B2), 961–966.

Popp, T., and Kern, H., 1994, The influence of dry and water saturated cracks on seismic velocities of crustal rocks—A comparison of experimental data with theoretical models: *Surveys in Geophysics*, v. 15, p. 443–465, https://doi.org/10.1007/BF00690169.

Regan, J., & Anderson, D. L. (1984). Anisotropic models of the upper mantle. *Physics of the Earth and Planetary Interiors*, *35*(4), 227-263.

Richards, M., Contreras-Reyes, E., Lithgow-Bertelloni, C., Ghiorso, M., & Stixrude, L. (2013). Petrological interpretation of deep crustal intrusive bodies beneath oceanic hotspot provinces. *Geochemistry, Geophysics, Geosystems*, *14*(3), 604-619.

Robinson, A. H., Peirce, C., & Funnell, M. J. (2018). Construction and subduction of the Louisville Ridge, SW Pacific-insights from wide-angle seismic data modelling. *Geophys. J. Int*, *215*(3), 2222-2245.

Rotzien, J. R., Hernández-Molina, F. J., Fonnesu, M., & Thieblemont, A. (2022), Deepwater sedimentary processes. In *Deepwater Sedimentary Systems* (pp. 179-202). Elsevier.

Russo, R. M., Gallego, A., Comte, D., Mocanu, V. I., Murdie, R. E., & VanDecar, J. C. (2010). Source-side shear wave splitting and upper mantle flow in the Chile Ridge subduction region. *Geology*, *38*(8), 707-710.

Sallarès, V., Charvis, P., Flueh, E. R., & Bialas, J. (2003). Seismic structure of Cocos and Malpelo Volcanic Ridges and implications for hot spot-ridge interaction. *Journal of Geophysical Research: Solid Earth*, *108*(B12).

Seton, M., Müller, R. D., Zahirovic, S., Gaina, C., Torsvik, T., Shephard, G., ... and Chandler, M. (2012). Global continental and ocean basin reconstructions since 200 Ma. *Earth-Science Reviews*, *113*(3-4), 212-270.

Seton, M., Mueller, R. D., Zahirovic, S., Williams, S., Wright, N. M., Cannon, J., ... and McGirr, R. (2020), A global data set of present-day oceanic crustal age and seafloor spreading parameters. *Geochemistry, Geophysics, Geosystems*, *21*(10), e2020GC009214.

Sleep, N. H. (1975). Formation of oceanic crust: Some thermal constraints. *J. Geophys. Res.*, *80*(29), 4037-4042.

Shearer, P., and Orcutt, J. (1985). Anisotropy in the oceanic lithosphere—theory and observations from the Ngendei seismic refraction experiment in the south-west Pacific. *Geophys. J. Int.*, *80*(2), 493-526.

Skemer, P., and Hansen, L. N. (2016). Inferring upper-mantle flow from seismic anisotropy: An experimental perspective. *Tectonophysics*, 668-669, 1–14. https://doi.org/10.1016/j.tecto.2015.12.003

Spudich, P., and Orcutt, J. (1980), Petrology and porosity of an oceanic crustal site: Results from wave form modeling of seismic refraction data. *J. Geophys. Res.: Solid Earth*, *85*(B3), 1409–1433. https://doi.org/10.1029/jb085ib03p01409

Staudigel, H., & Schmincke, H. U. (1984). The pliocene seamount series of la palma/canary islands, *J. Geophys. Res.,: Solid Earth*, *89*(B13), 11195-11215.

Stratford, W., Peirce, C., Paulatto, M., Funnell, M., Watts, A. B., Grevemeyer, I., & Bassett, D. (2015). Seismic velocity structure and deformation due to the collision of the Louisville Ridge with the Tonga-Kermadec Trench. *Geophys. J. Int.*, *200*(3), 1503-1522.

Straume, E.O., Gaina, C., Medvedev, S., Hochmuth, K., Gohl, K., Whittaker, J. M., et al. (2019). GlobSed: Updated total sediment thickness in the world's oceans. *Geochemistry, Geophysics, Geosystems,* 20. DOI: 10.1029/2018GC008115

Tenzer, R., and Gladkikh, V. (2014), Assessment of density variations of marine sediments with ocean and sediment depths. *The Scientific World Journal*, *2014*(1), 823296.

Toomey, D. R., Hooft, E. E., & Wilcock, W. S. (2007). Is skew of mantle upwelling beneath spreading centers globally significant? Observations (EPR), hints (MAR) and predictions (Juan de Fuca). In *AGU Fall Meeting Abstracts* (Vol. 2007, pp. T33B-1359).

Trummer, I. (2002). *S-wave processing and interpretation of wide-angle seismic refraction data, Malpelo Ridge, Eastern Panama Basin* (Doctoral dissertation University of Kiel, Germany).

VanderBeek, B. P., Toomey, D. R., Hooft, E. E. E., & Wilcock, W. S. D. (2016). Segmentation of mid-ocean ridges attributed to oblique mantle divergence. *Nature Geoscience*, 9(8), 636–642. https://doi.org/10.1038/ngeo2745

Toomey, D. R., Jousselin, D., Dunn, R. A., Wilcock, W. S. D., & Detrick, R. S. (2007). Skew of mantle upwelling beneath the East Pacific rise governs segmentation. *Nature*, 446(7134), 409–414. https://doi.org/10.1038/nature05679

Trummer, I. (2002), S-wave processing and interpretation of wide-angle seismic refraction data, Malpelo ridge, eastern Panama basin. (*Doctoral dissertation*). *University of Kiel.*

Yang, L., and Li, Y. (2023). Tectonic deformation at the outer rise of subduction zones. *Geophys. J. Int*, *232*(3), 1533-1544.

Waff, H. S., and Faul, U. H. (1992). Effects of crystalline anisotropy on fluid distribution in ultramafic partial melts. *J. Geophys. Res.: Solid Earth*, *97*(B6), 9003-9014.

Walther, C. H. (2003). The crustal structure of the Cocos ridge off Costa Rica. *Journal of Geophysical Research: Solid Earth*, *108*(B3).

Wagner, L. S., Caddick, M. J., Kumar, A., Beck, S. L., & Long, M. D. (2020), Effects of oceanic crustal thickness on intermediate depth seismicity. *Frontiers in Earth Science*, *8*, 244.

Wang, X.-Q., Schubnel, A., Fortin, J., David, E.C., Guéguen, Y., and Ge, H.-K., 2012, High V_p/V_s ratio: Saturated cracks or anisotropy effects?: *Geophys. Res. Lett.*, v. 39, L11307, doi.org/10.1029/2012GL051742

Wang, D., Wang, L., Zhang, R., Cai, N., Zhang, J., Chen, P., and Cao, Y. (2022), Mantle Wedge Water Contents Estimated From Ultrasonic Laboratory Measurements of Olivine-Antigorite Aggregates. *Geophys. R. Lett.*, *49*(10), e2022GL098226.

Watts, A. B., Grevemeyer, I., Shillington, D. J., Dunn, R. A., Boston, B., and Gómez de La Peña, L. (2021). Seismic structure, gravity anomalies and flexure along the Emperor Seamount chain. *J. Geophys. Res.,: Solid Earth*, *126*(3), e2020JB021109.

Weigel, W., and I. Grevemeyer (1999), The Great Meteor seamount: Seismic structure of a submerged intraplate volcano, *J. Geodyn*., 28, 27–40.

White, R.S., McKenzie, D. and O'Nions, K., (1992), Oceanic crustal thickness from seismic measurements and rare earth element inversions, *J. Geophys. Res.,* **97**(B13), 19 683–19 715.

White, R. S., & Stephen, R. A. (1980), Compressional to shear wave conversion in oceanic crust. *Geophys. J. Int.*, *63*(2), 547–565. https://doi.org/10.1111/j.1365-246x.1980.tb02637.x

Wolfe, C. J., McNutt, M. K., & Detrick, R. S. (1994). The Marquesas archipelagic apron: Seismic stratigraphy and implications for volcano growth, mass wasting, and crustal underplating. *J. Geophys. Res.,: Solid Earth*, *99*(B7), 13,591-13,608.

Worthington, T. J., Hekinian, R., Stoffers, P., Kuhn, T., & Hauff, F. (2006). Osbourn Trough: Structure, geochemistry and implications of a mid-Cretaceous paleospreading ridge in the South Pacific. *Earth and Planetary Science Letters*, *245*(3-4), 685-701.

Xu, C., Dunn, R. A., Watts, A. B., Shillington, D. J., Grevemeyer, I., Gomez de la Pena, L., & Boston, B. B. (2022). A seismic tomography, gravity, and flexure study of the crust and upper mantle structure of the Emperor Seamounts at Jimmu guyot. *J. Geophys. Res: Solid Earth*, *127*(6), e2021JB023241.

Zhang, S., and Karato, S. I. (1995). Lattice preferred orientation of olivine aggregates deformed in simple shear. *Nature*, *375*(6534), 774-777.

Zoeppritz, K. (1919). On reflection and transmission of seismic waves by surfaces of discontinuity. *Nachrichten von der Königlichen Gesellschaft der Wissenschaften zu Göttingen, Mathematisch-physikalische Klasse*, 66-84.

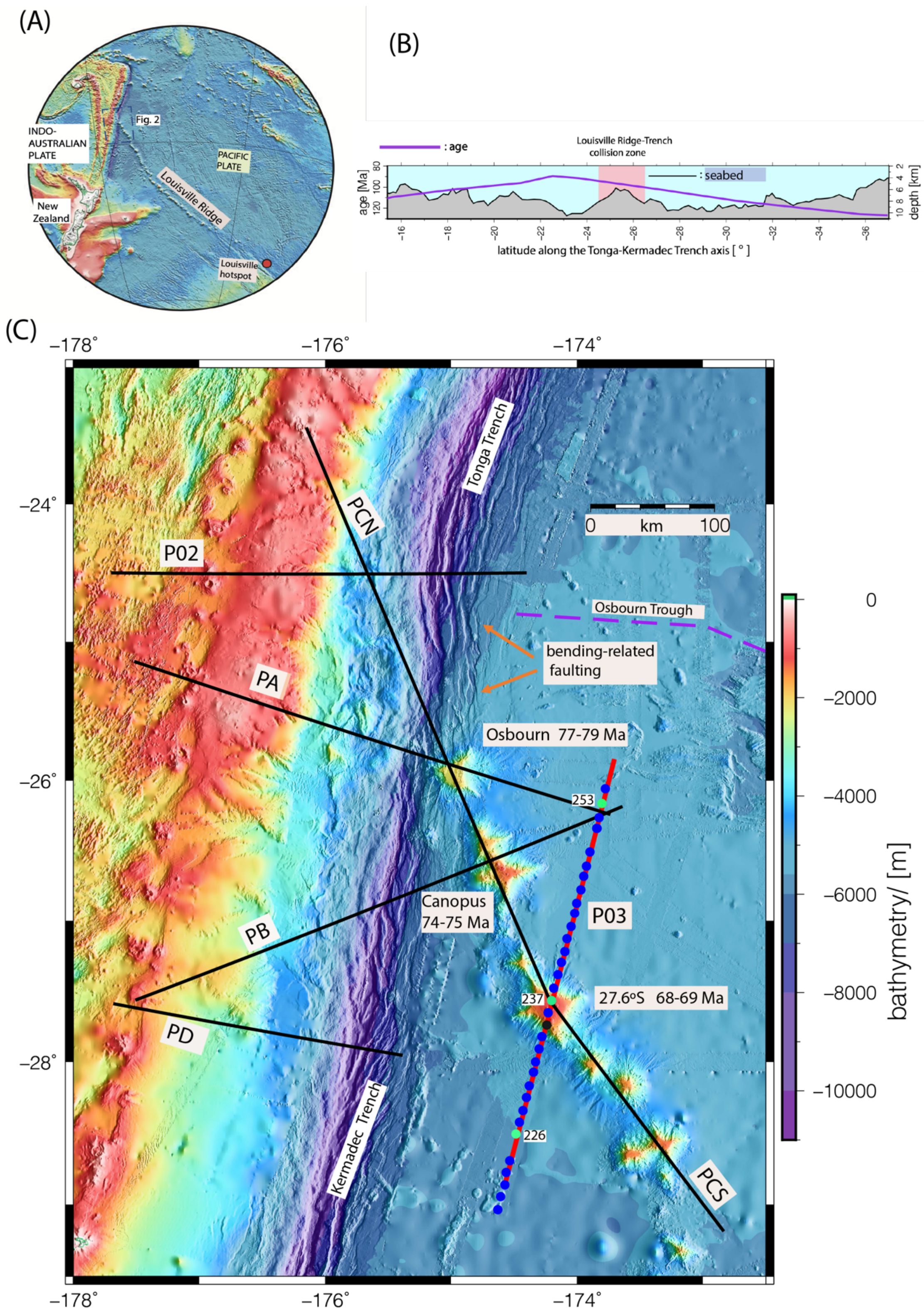

Fig. 1. **(A)** Geodynamic setting of the Pacific, Antarctic, and Indo-Australian Plates. The Louisville Ridge is an ~4,300 km-long hotspot track that formed by the interaction of the Pacific Plate with the Louisville hotspot

(red dot) located near the intersection of the Eltanin Fracture Zone with the SW Pacific–Antarctica spreading center (e.g., Watts et al., 1988). The Pacific Plate approaches the Tonga-Kermadec Trench at a convergence rate of 150 km/Myr (Lonsdale, 1986). **(B)** Tonga-Kermadec Trench axis depth taken from the global bathymetric grid of Ryan et al. (2009). The age of the oceanic Pacific Plate at the trench axis was taken from the global grid of Mueller et al. (2008). **(C)** Global satellite observations and swath bathymetry seabed topography of the Tonga-Kermadec Trench-Louisville Ridge collision zone (Ryan et al., 2009). The Osbourn seamount is the oldest remaining seamount prior to collision with the Indo-Australian Plate. Approximate basement ages for the seamounts are based on radiometric age dating of dredged rock samples (Koppers et al., 2004; 2011). The solid black lines represent the wide-angle seismic profiles reported by Stratford et al. (2015; profile PA), Funnell et al. (2017; profile PB), Robinson et al. (2018; profile PC, split into north and south parts annotated PCN and PCS), and Contreras-Reyes et al. (2011; profile P02). Profile PD was a multichannel seismic reflection profile only, reported by Funnell et al. (2017). The red line depicts the wide-angle seismic profile P03 modelled in this study, while the blue dots indicate the locations of the 33 OBH/S stations. Green dots with station numbers indicate the three OBH's (253, 237, and 226) shown in Figs. 3-5.

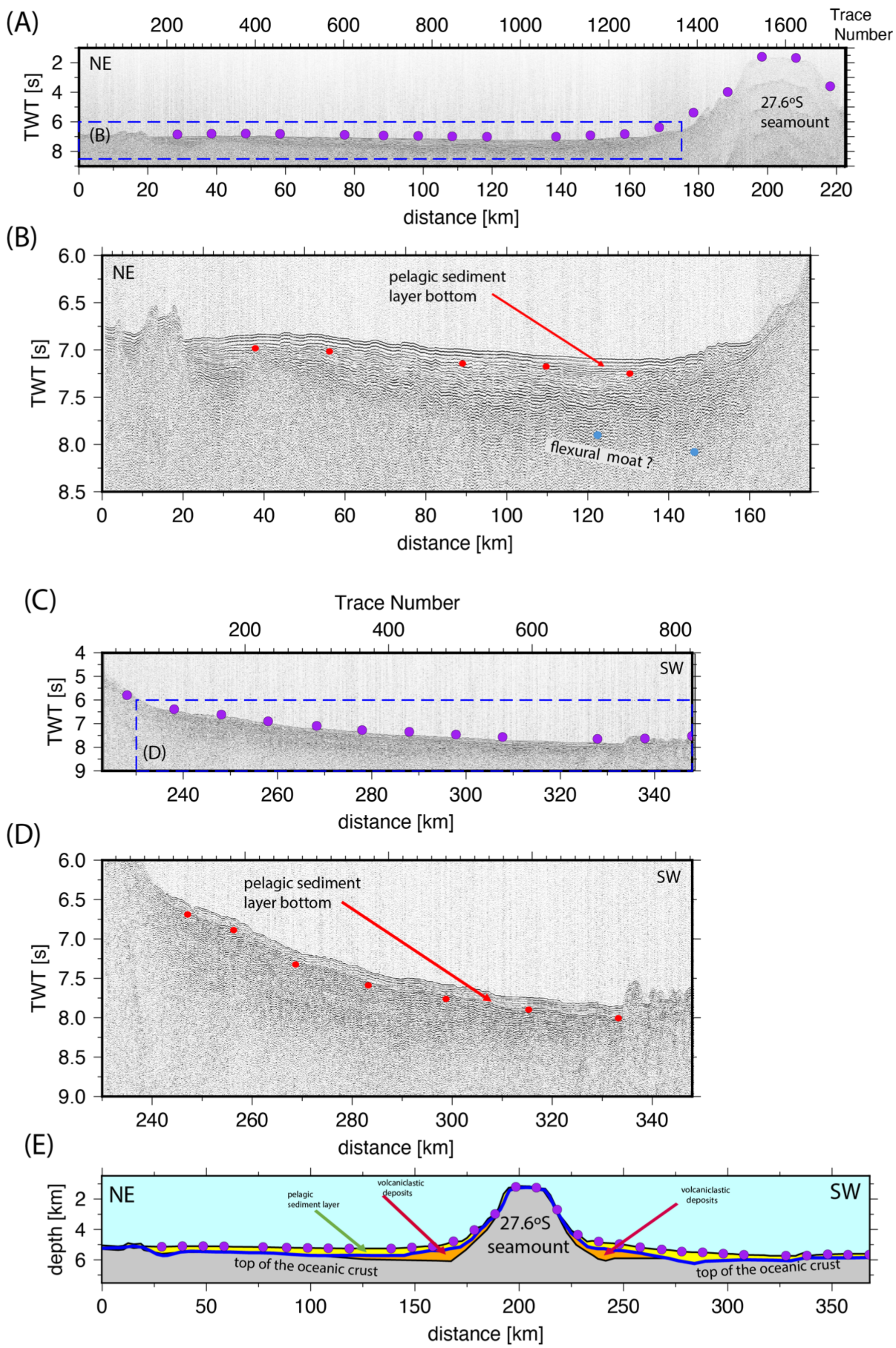

Fig. 2. Seismic reflection data along profile P03. **(A)** Section of profile to the NE of the 27.6ºS seamount. **(B)** Zoom-in as shown by the blue dashed box in (A). **(C)** Section of profile to the SW of the 27.6ºS seamount. **(D)**

Zoom-in as shown by the blue dashed box in (C). (A)-(D) are plotted in two-way-travel (TWT) time. The average pelagic sediment thickness is 0.1-0.15 TWT, ~0.35-0.5 km. **(E)** Main reflectors and bathymetry converted from TWT to depth using the 2-D V_p model of Contreras-Reyes et al. (2010). Pelagic sediments and volcaniclastic deposits are differentiated by V_p ranges of 1.6-1.9 km/s and >2.0-4.5 km/s, respectively. The flexural moat geometry is based on the 2-D V_p model of Contreras-Reyes et al. (2010). Purple dots depict the location of the OBH/S shown in (A), (C) and (E). Red dots mark the bottom of the pelagic sediment layer in (B) and (D).

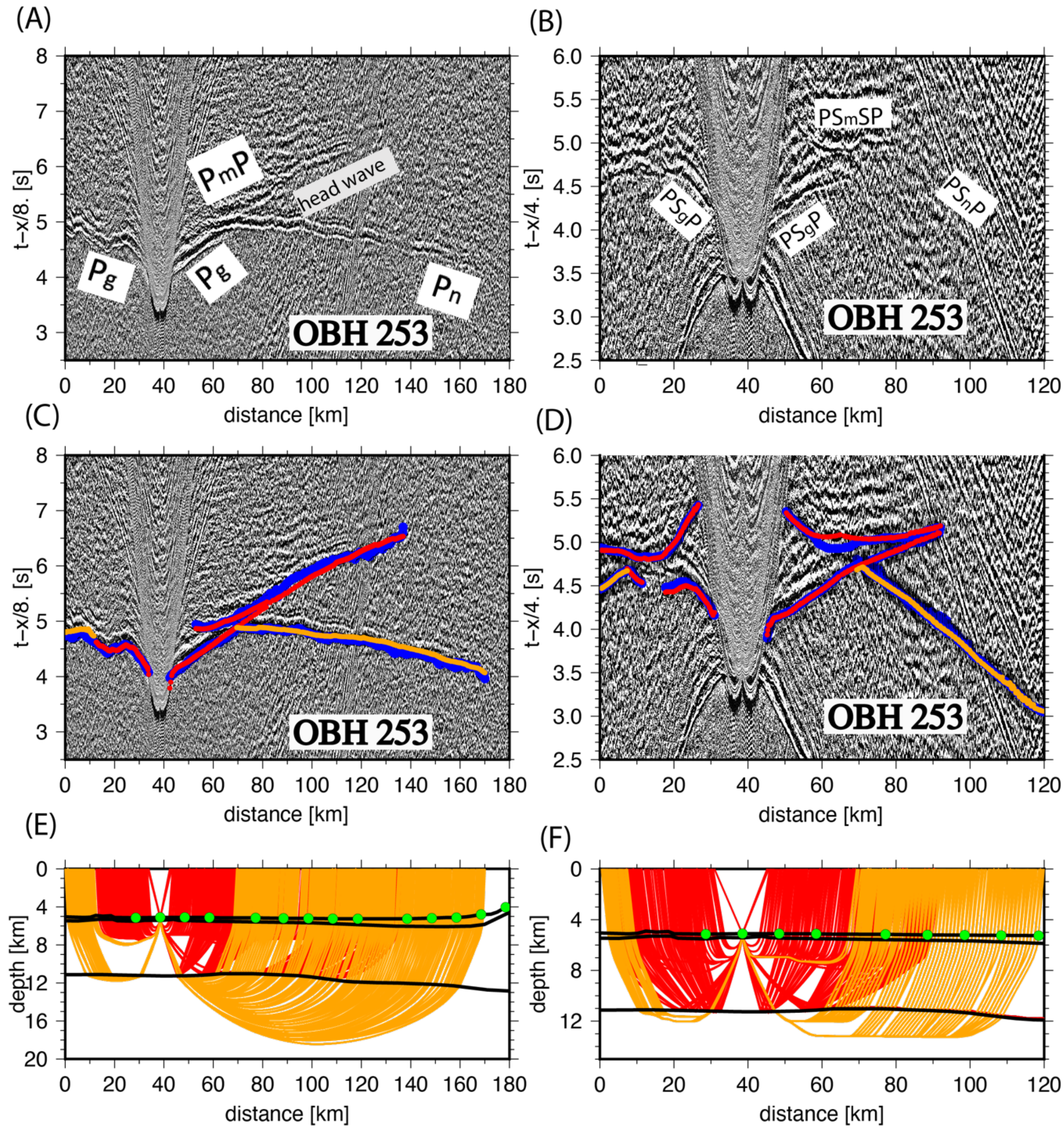

Fig. 3. (A) Seismic record section for OBH 253, plotted at a reduction velocity of 8.0 km/s to highlight crustal (P_g) and upper (P_n) mantle refractions. The Moho reflections (P_mP) were used to constrain the crustal thickness (Contreras-Reyes et al., 2010). **(B)** Plotted at a reduction velocity of 4.0 km/s to highlight converted P-S-P crustal (PS_gP) and mantle (PS_nP) refractions. Mode converted P-S-P Moho reflections (PS_mSP) were also recorded at some stations. In parts (A) and (B) phase identifications are annotated. Predicted travel times, represented by orange and red curves, are compared with the corresponding interpreted picks (blue curves) which are scaled to the pick uncertainty for **(C)** P-wave and **(D)** S-wave modelling. Predicted travel times are calculated using the 2-D V_p (Fig. 7A) and V_s (Fig. 7B) inversion models. Ray-tracing of the **(E)** P-wave and **(F)** converted P-S-P-waves. Green dots in (E) and (F) mark OBH/S locations.

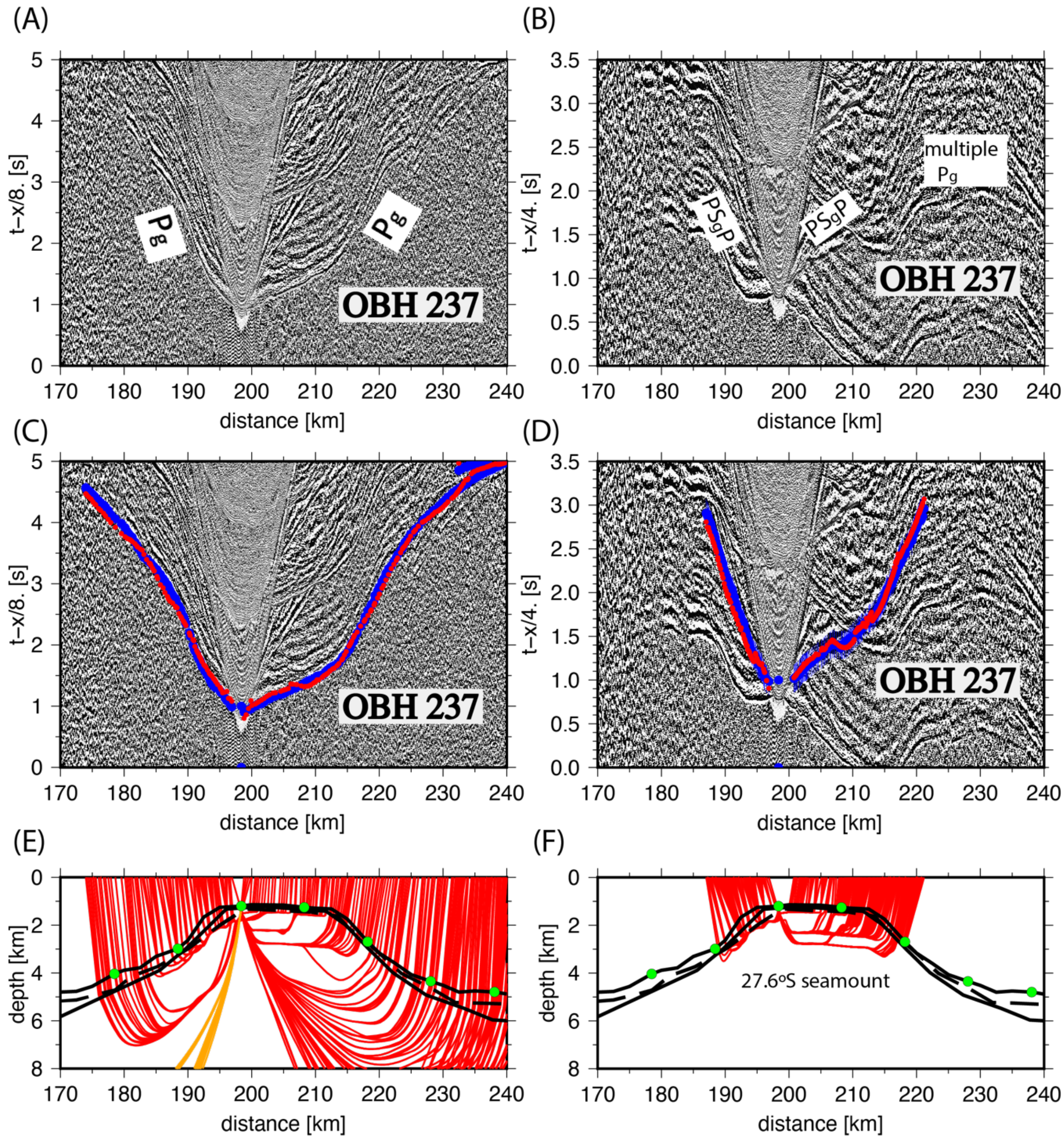

Fig. 4. **(A)** Seismic record section for OBH 237, plotted at a reduction velocity of 8.0 km/s to highlight crustal (P_g) refractions. **(B)** Plotted at a reduction velocity of 4.0 km/s to highlight converted P-S-P crustal refractions (PS_gP). In parts (A) and (B) phase identifications are annotated. Predicted travel times, represented by red curves, are compared with the corresponding interpreted picks (blue curves) which are scaled to the pick uncertainty for **(C)** P-wave and **(D)** S-modelling. Predicted travel times are calculated using the 2-D V_p (Fig. 7A) and V_s (Fig. 7B) inversion models. Ray-tracing of the **(E)** P-wave and **(F)** converted P-S-P-waves. Green dots in (E) and (F) mark OBH/S locations.

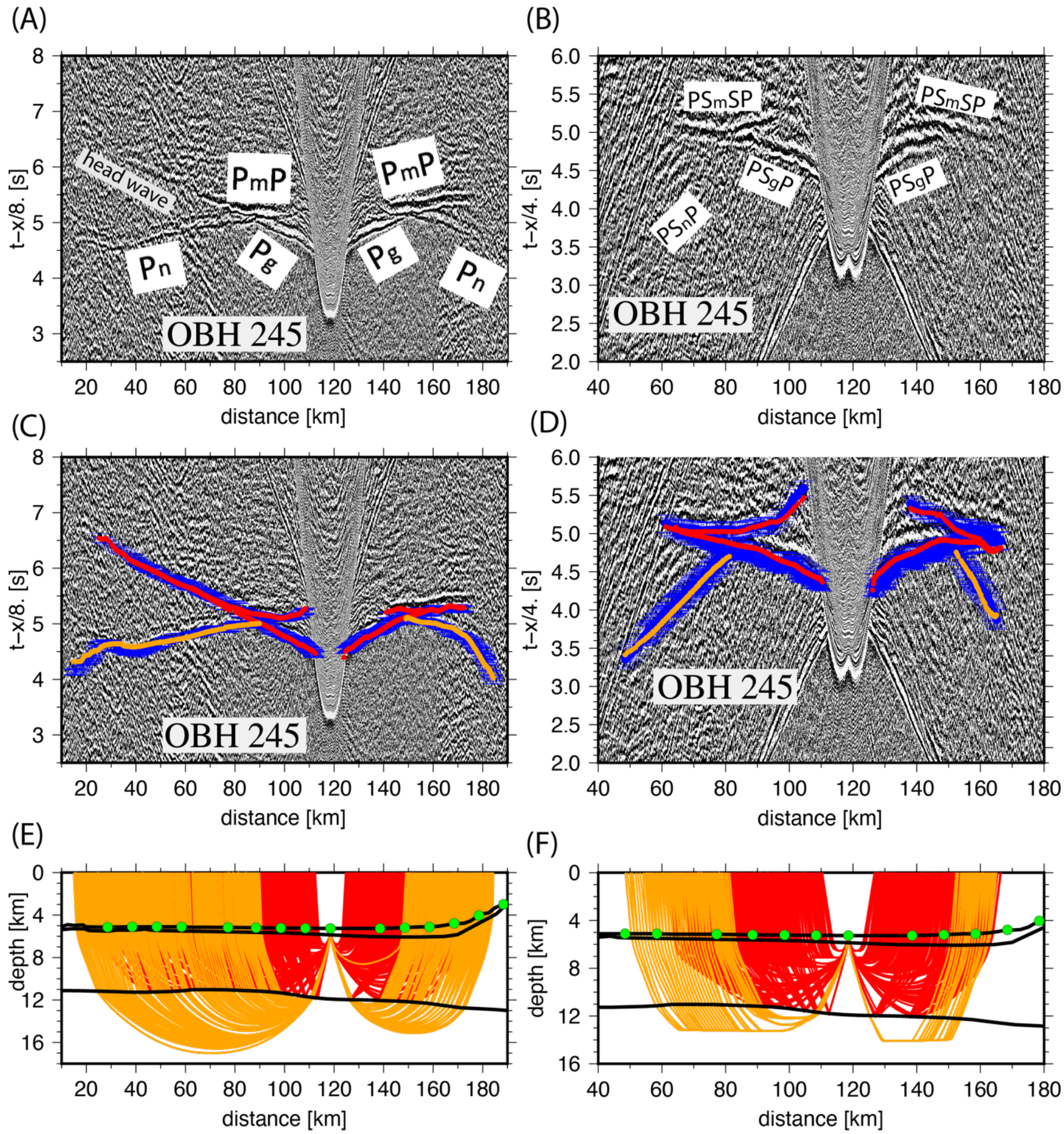

Fig. 5. **(A)** Seismic record section for OBH 245, plotted at a reduction velocity of 8.0 km/s to highlight crustal upper mantle phases. **(B)** Plotted at a reduction velocity of 4.0 km/s to highlight converted P-S-P phases. In parts (A) and (B) phase identifications are annotated. **(C)** Predicted travel times, represented by orange and red

curves, are compared with the corresponding interpreted picks (blue curves) which are scaled to the pick uncertainty for **(C)** P-wave and **(D)** S-modelling. Predicted travel times are calculated using the 2-D V_p (Fig. 7A) and V_s (Fig. 7B) inversion models. Ray-tracing of the **(E)** P-wave and **(F)** converted P-S-P-waves. Green dots in (E) and (F) mark OBH/S locations.

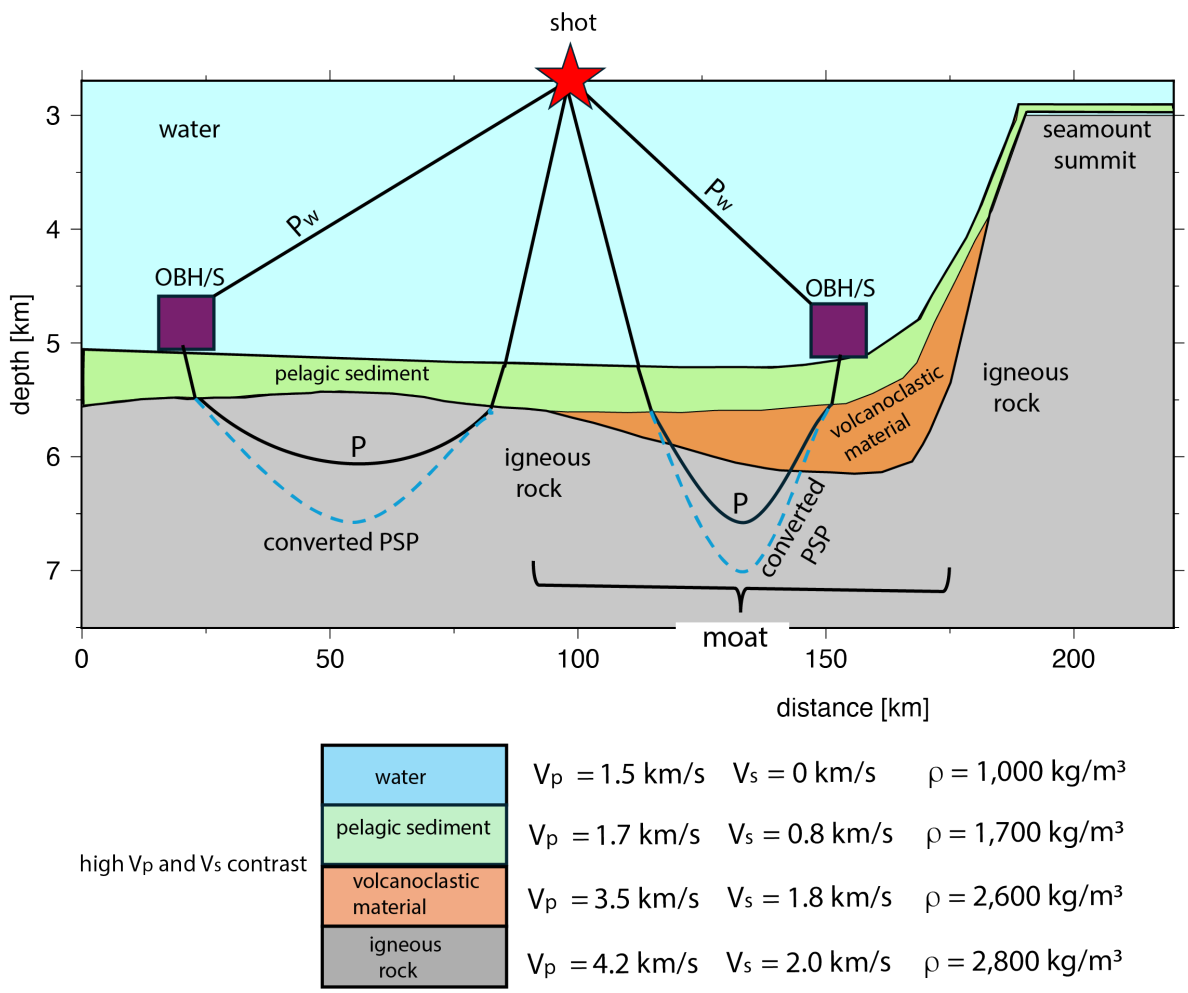

Fig. 6. Schematic diagram showing converted P-S-P-waves. Reference values for V_p and V_s, and densities (ρ) are shown to highlight the higher velocity and density contrast at the sediment/basement interface compared with the water/sediment interface. Typical V_p, V_s, and ρ values are based on Fulthorpe et al. (1989), Caress et

al. (1995) and Christeson et al. (2019). Adjacent to the flexural moat, the P-to-S-wave conversion is more likely to occur at the pelagic sediment/igneous basement interface, while in the flexural moat it is more likely to occur at the pelagic sediment/volcanoclastic interface that maximizes the acoustic impedance contrast. Seismic energy propagates as a P-wave through the water and pelagic sediment layer (both upward and downward) and as an S-wave through the volcaniclastic material, crust, and mantle. P_w: direct P-wave through the water.

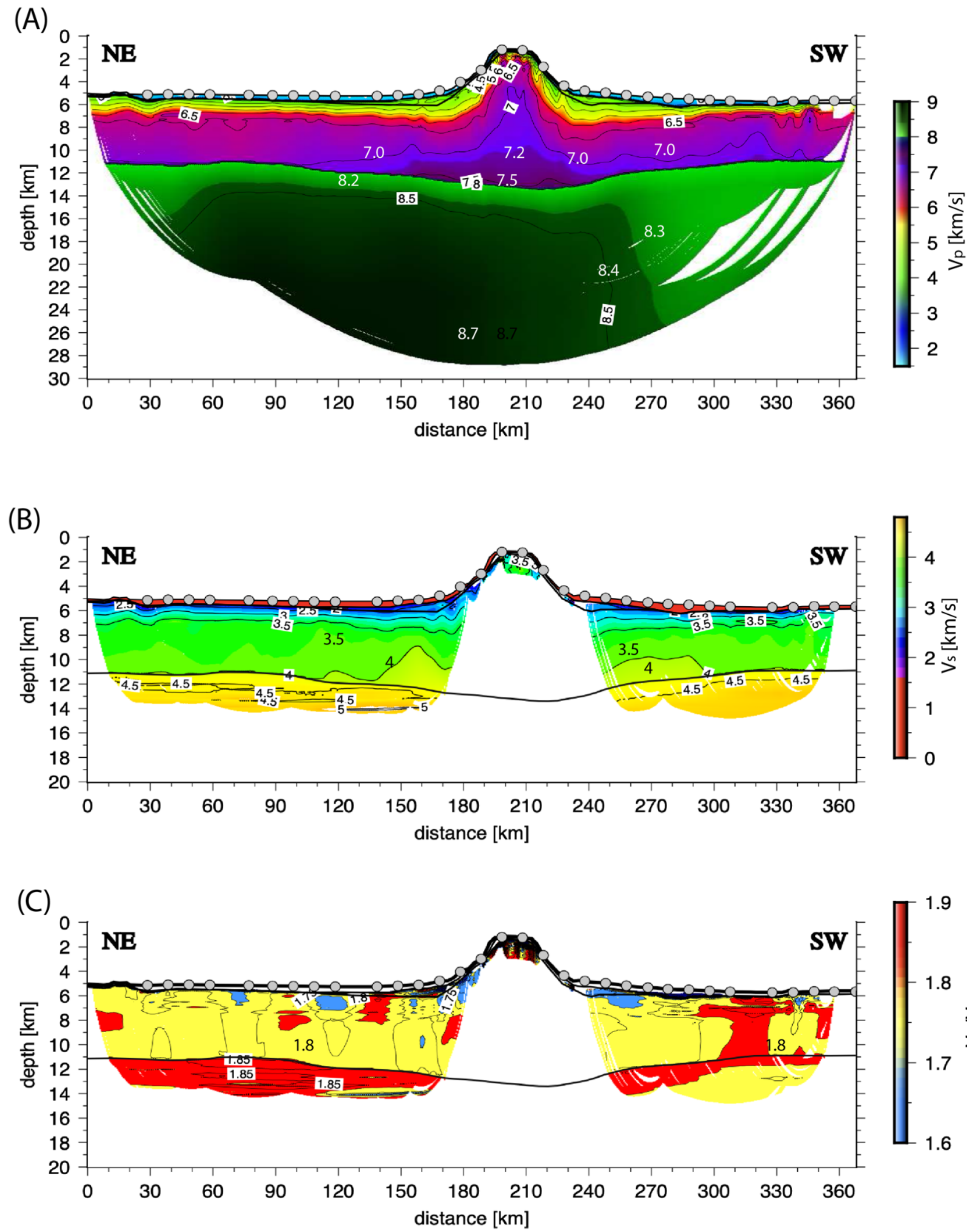

Fig. 7. Final **(A)** P-wave and **(B)** S-wave velocity tomographic inversion models masked by the ray coverage (see Fig. 8 and Supporting Information). **(C)** Resultant 2-D V_p/V_s model derived from (A) and (B).

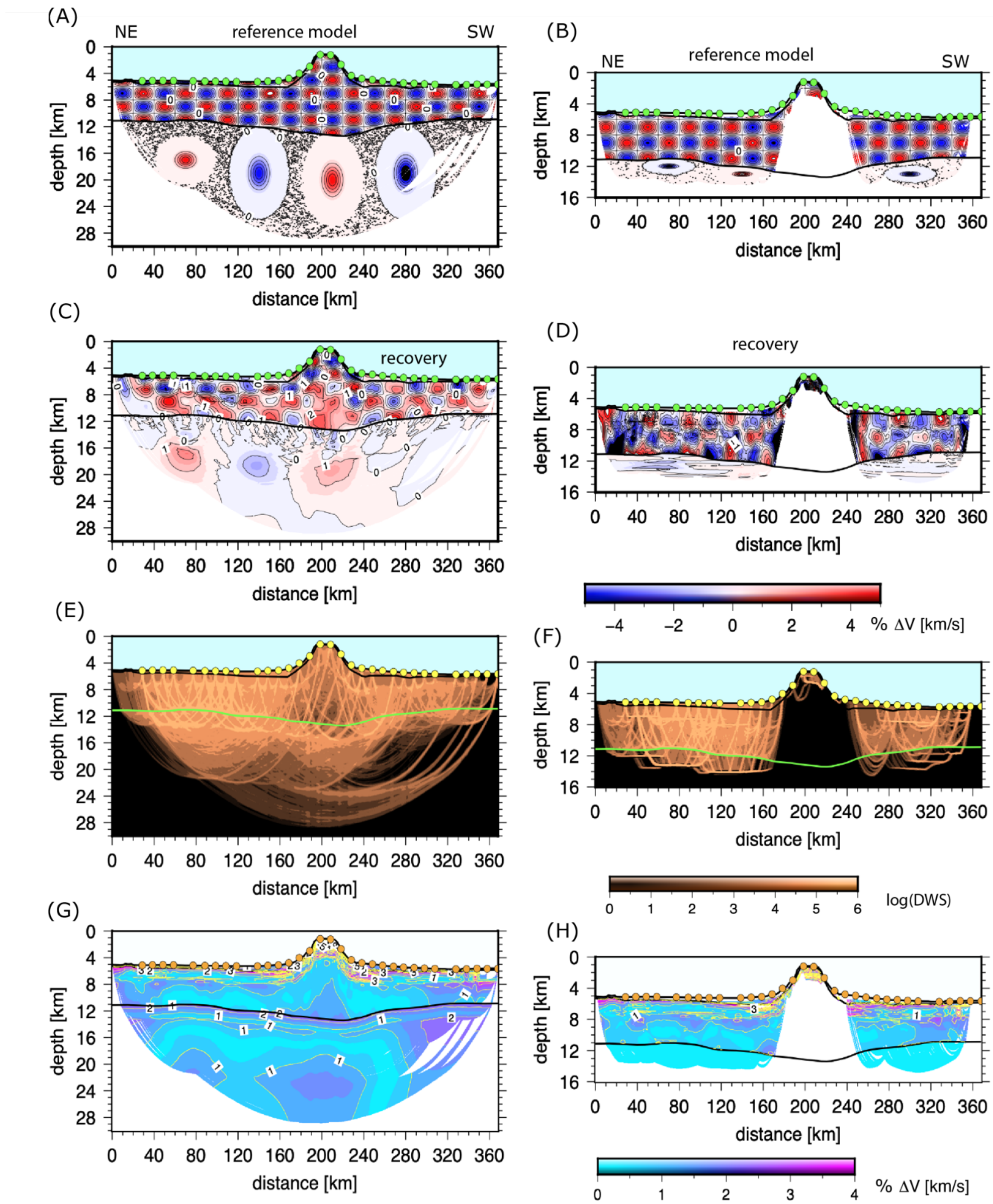

Fig. 8. Results of checkerboard testing. Synthetic reference velocity model for **(A)** V_p and **(B)** V_s, consisting of velocity anomalies of 40 km x 4 km with maximum velocity amplitudes of ± 5% for the oceanic crust. For the upper mantle, we use Gaussian anomalies superimposed onto the final velocity model shown in Figs. 7A and 7B. Recovery for the **(C)** V_p and **(D)** V_s models. See Supporting Information for details and further resolution

tests. Derivative Weight Sum (DWS) in logarithmic scale for rays traveling through the **(E)** V_p and **(F)** V_s models. Percentage standard deviation of the **(G)** V_p and **(H)** V_s models. See enlarged version of these figures in the Supporting Information.

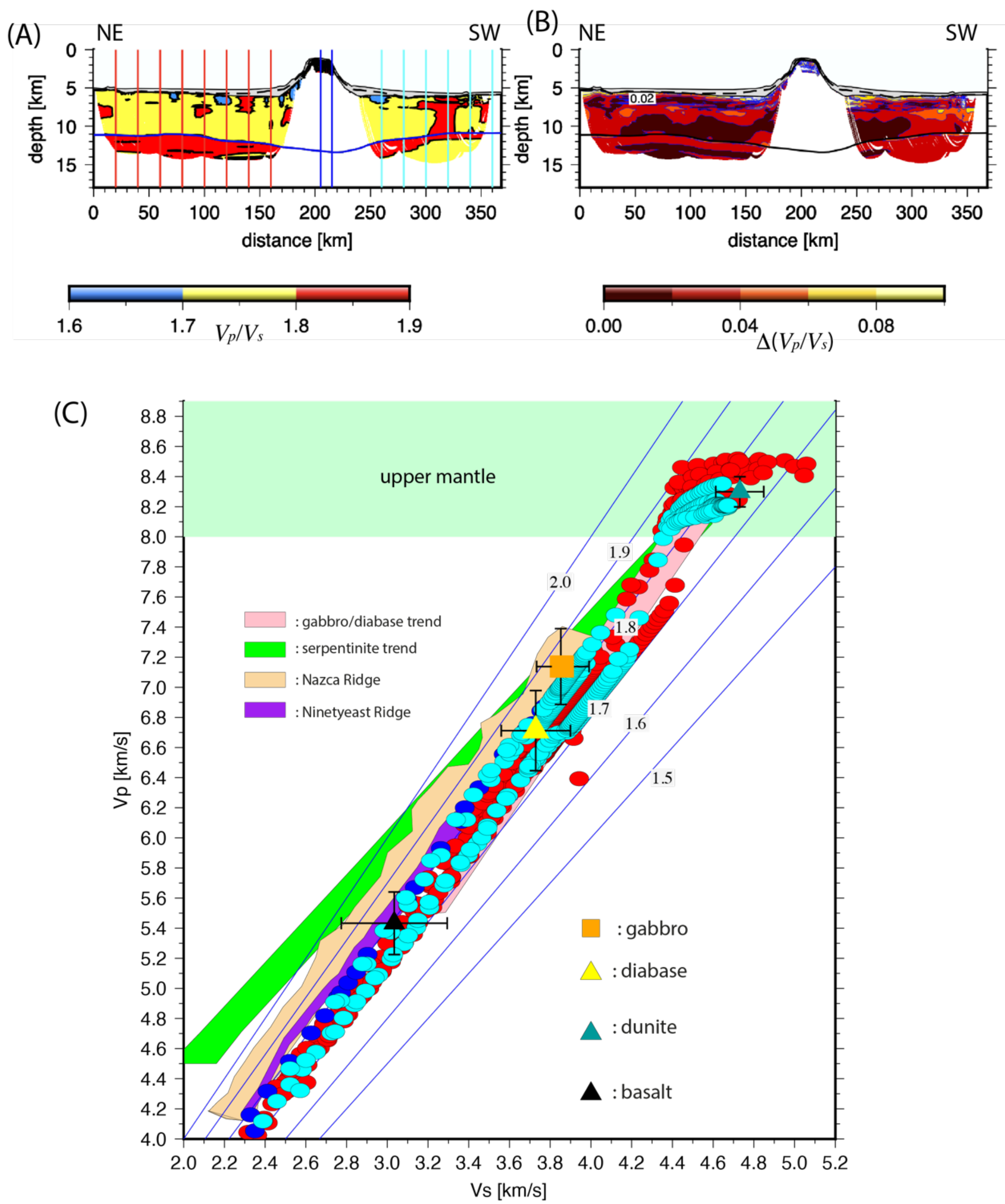

Fig. 9. (A) 2-D V_p/V_s model and its **(B)** $\Delta\left(\frac{V_p}{V_s}\right)$ uncertainties (see Supporting Information)**. (C)** Paths of constant V_p/V_s ratio (blue lines), which form straight lines in the V_p -V_s plane, are plotted at intervals of 0.1. The V_p and

V_s values for gabbro, diabase, dunite, and basalt were determined at 200 MPa by Christensen (1996). The trends of serpentinite and gabbro/diabase resulted from the optimal alignment of in-situ seismic velocities and laboratory measurements, as published by Carlson and Miller (2003). The paired (V_p, V_s) values, depicted as red, blue, and cyan ellipses, were extracted from the 2-D V_p and V_s models at the corresponding horizontal locations indicated in (A). The semi-minor and semi-major axes of each ellipse is taken as the average V_p and V_s uncertainty (see Figs. 8G and 8H).

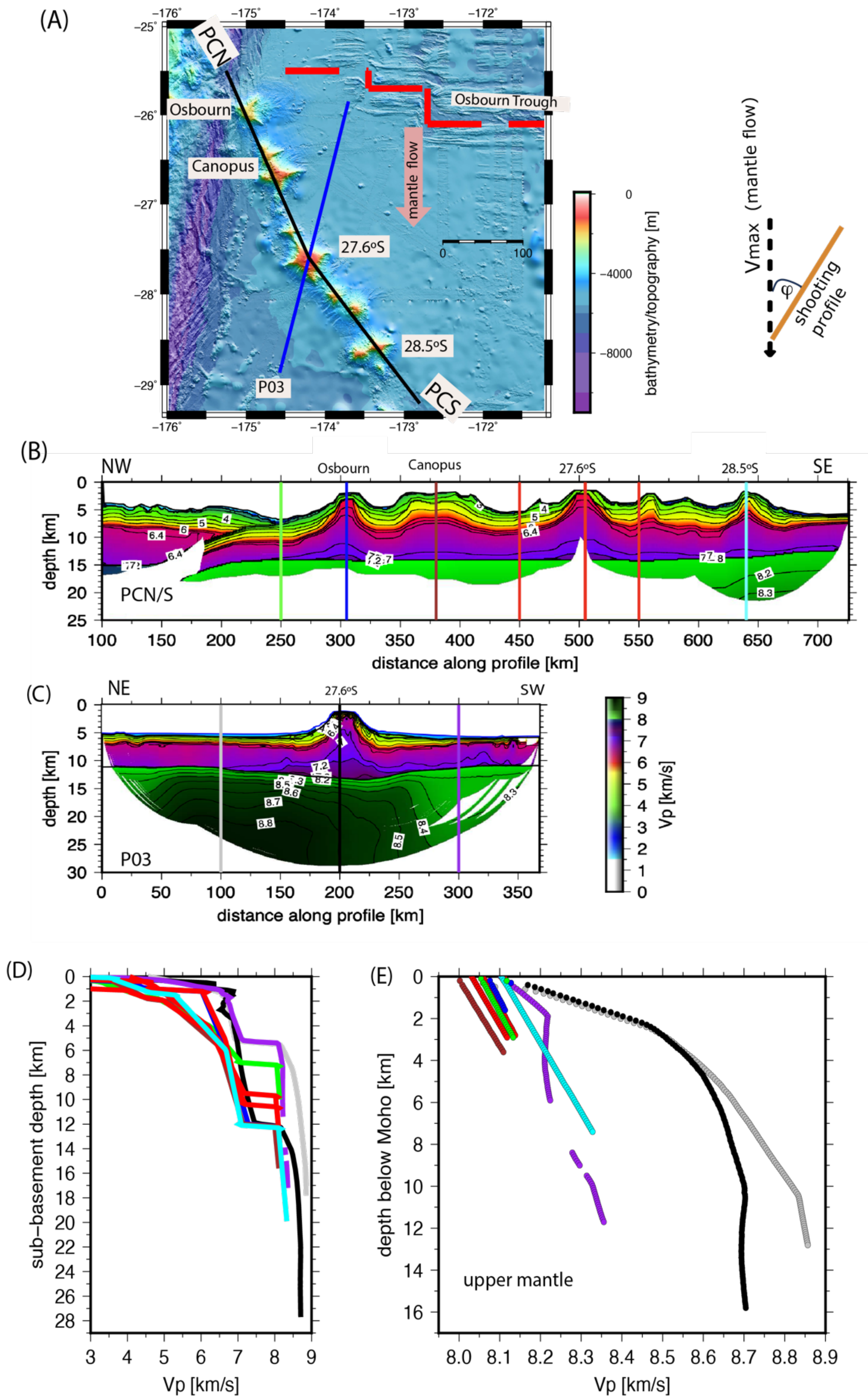

Fig. 10. **(A)** Location map for profiles PC (annotated in south and north parts – PCS and PCN; Robinson et al., 2018) and P03 (Fig. 1). Seismic profile P03 is oriented at an angle (φ) ~20º relative to the expected direction of

mantle flow, while profile PCS runs at an angle of ~50º. V_p models along **(B)** PCS (Robinson et al., 2018) and **(C)** P03. V_p profiles plotted as a function depth below **(D)** basement and **(E)** Moho, respectively, for the models shown in **(B)** and **(C).**

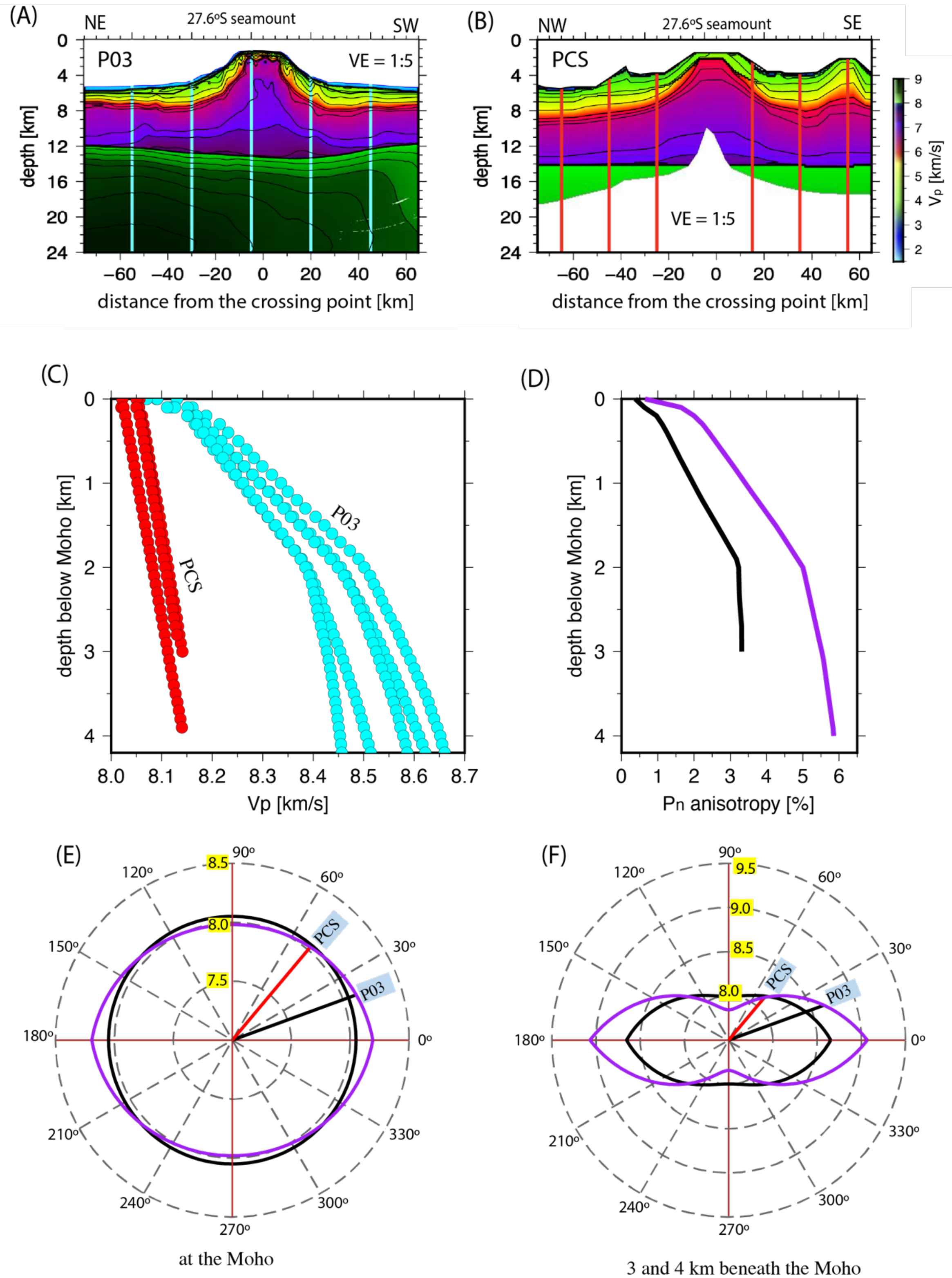

Fig. 11. 2-D V_p model along **(A)** P03 and **(B)** PCS (Fig. 10A; Robinson et al., 2018) beneath the 27.6ºS seamount. **(C)** V_p profiles plotted as a function of depth below the Moho for comparison. **(D)** Maximum (purple

curve) and minimum (black curve) P_n anisotropic percentage (Eq. 2) as a function of depth. The anisotropic percentage was calculated using the bounding V_p-depth profiles shown in (C). **(E)** P_n velocity measured along profiles P03 and PCS at Moho depth showing the minimum (black ellipse) and maximum (purple ellipse) anisotropy. **(F)** The minimum P_n anisotropic percentage at 3 km below the Moho (black ellipse), and maximum P_n anisotropic percentage at 4 km below the Moho (purple ellipse) are illustrated. For (E) and (F), profiles P03 and PCS have an azimuth of ~20º (φ_1) and ~50º (φ_2) relative to the paleo spreading direction, respectively (see Fig. 10A). At a specified depth, the P_n velocity measurements at azimuths φ_1 and φ_2 enable the determination of the faster V_{max}, assumed to align parallel to the paleo spreading direction, and the slower V_{min}, oriented perpendicular to it (see Eqs. 3-5).

TECTONOPHYSICS

Supporting Information for

V_p/V_s structure and P_n anisotropy across the Louisville Ridge, seaward of the Tonga-Kermadec Trench

Eduardo Contreras-Reyes[1], Ingo Grevemeyer[2], Christine Peirce[3], and Sebastián Obando-Orrego[1]

[1]Departamento de Geofísica, Facultad de Ciencias Físicas y Matemáticas, Universidad de Chile, Santiago, Chile

[2]GEOMAR-Helmholtz Centre for Ocean Research, Kiel, Germany

[3]Department of Earth Sciences, Durham University, South Road, Durham, DH1 3LE, UK

1. Introduction

We present example seismic record sections for ocean-bottom hydrophones/seismographs (OBH/S) deployed along profile P03 which obliquely crosses the Louisville Ridge and is orientated sub-parallel to the Tonga-Kermadec Trench axis. For this experiment, we deployed 33 OBH/Ss along the ~368 km-long profile, each with a spacing of ~9 km (Fig. S1). The seismic source comprised a system of G-gun clusters with a total volume of 84 l which was operated at 3000 psi. The shot interval was 60 s (Grevemeyer and Flueh, 2008). Most of the instrument recordings are of good quality, showing clear signals at large offsets. Both P-wave and mode-converted P-to-S-to-P-waves have been recorded. In the following figures we show example seismic record sections with identified phases annotated, uncertainty estimates for both V_p and V_s models, resolution tests, and the density of ray coverage.

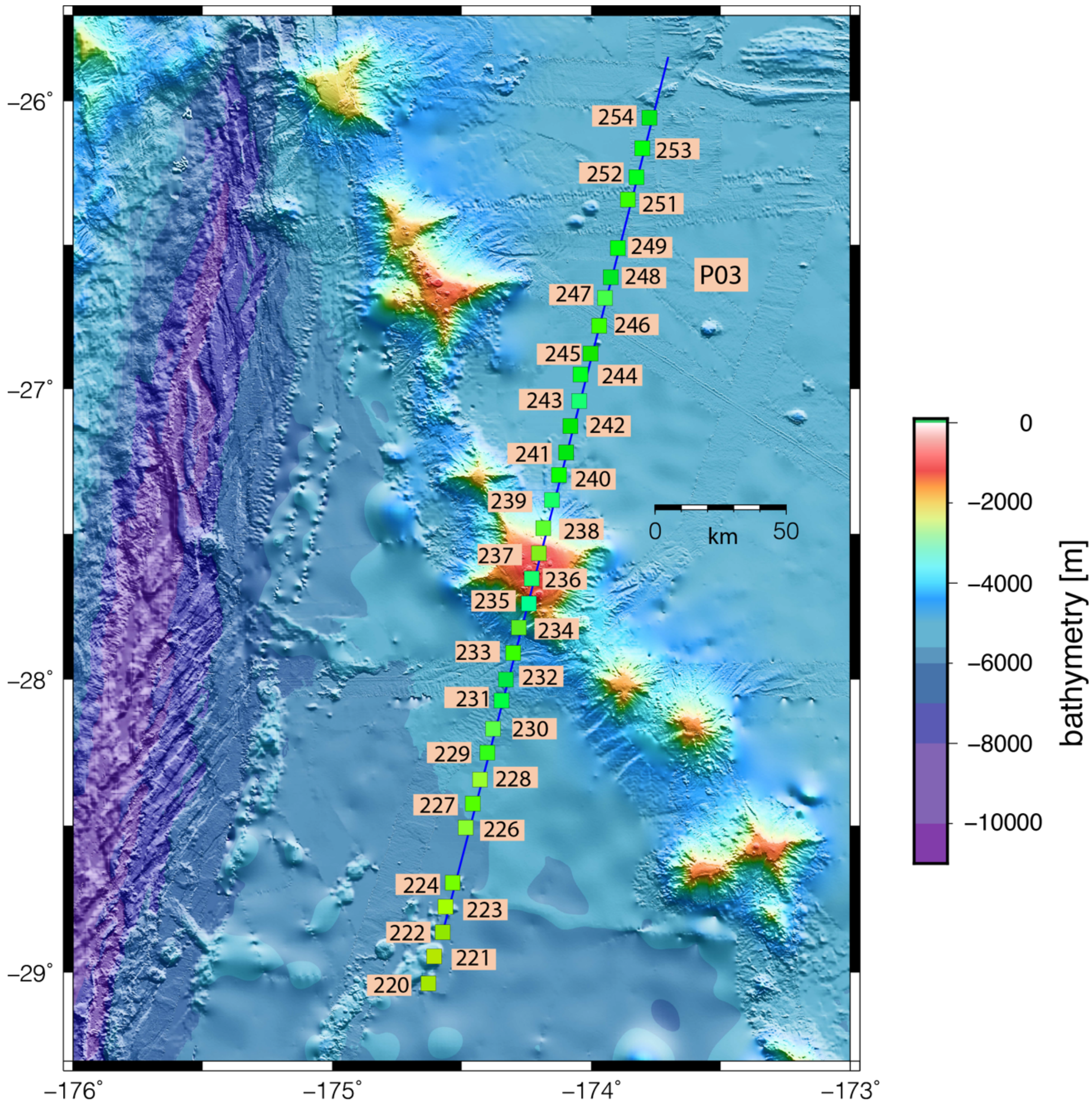

Fig. S1. Seismic profile P03, oriented sub-parallel to the Tonga-Kermadec Trench axis and crosses the Louisville Ridge at 27.6ºS seamount. Airgun shots are marked by the blue solid line and the locations of deployed OBH/Ss are marked by green dots with the station number annotated.

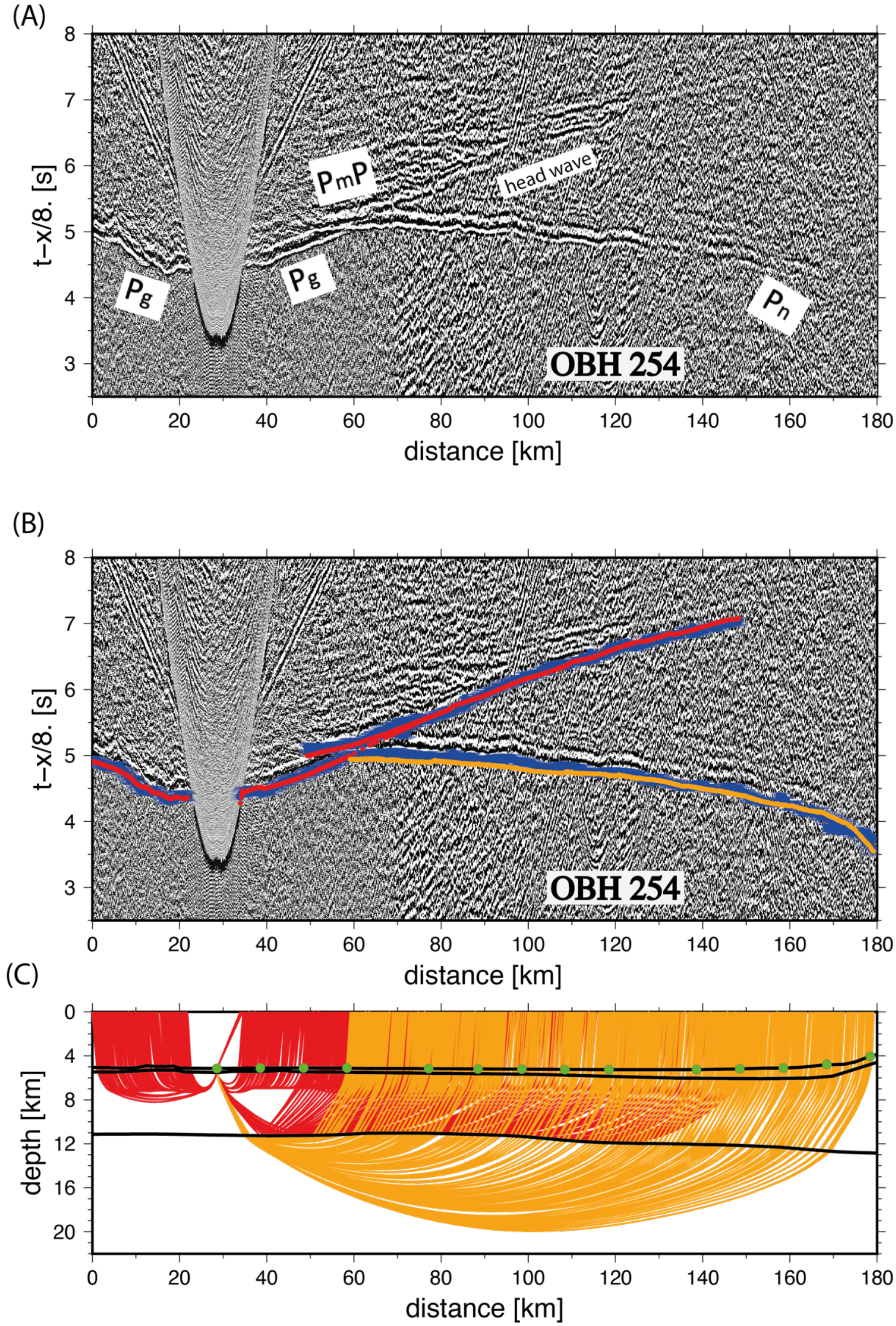

Fig. S2. (**A**) Wide-angle seismic data from OBH 254, plotted at a reduction velocity of 8 km/s and with crustal and mantle P-wave phases identified. (**B**) Predicted travel times are based on the 2-D V_p model shown in Fig. 7A. Blue bars corresponds to the travel time picks, scaled to the pick uncertainty. (**C**) Ray path diagram corresponding to the predicted travel times shown in (B). Green dots mark OBH/S locations.

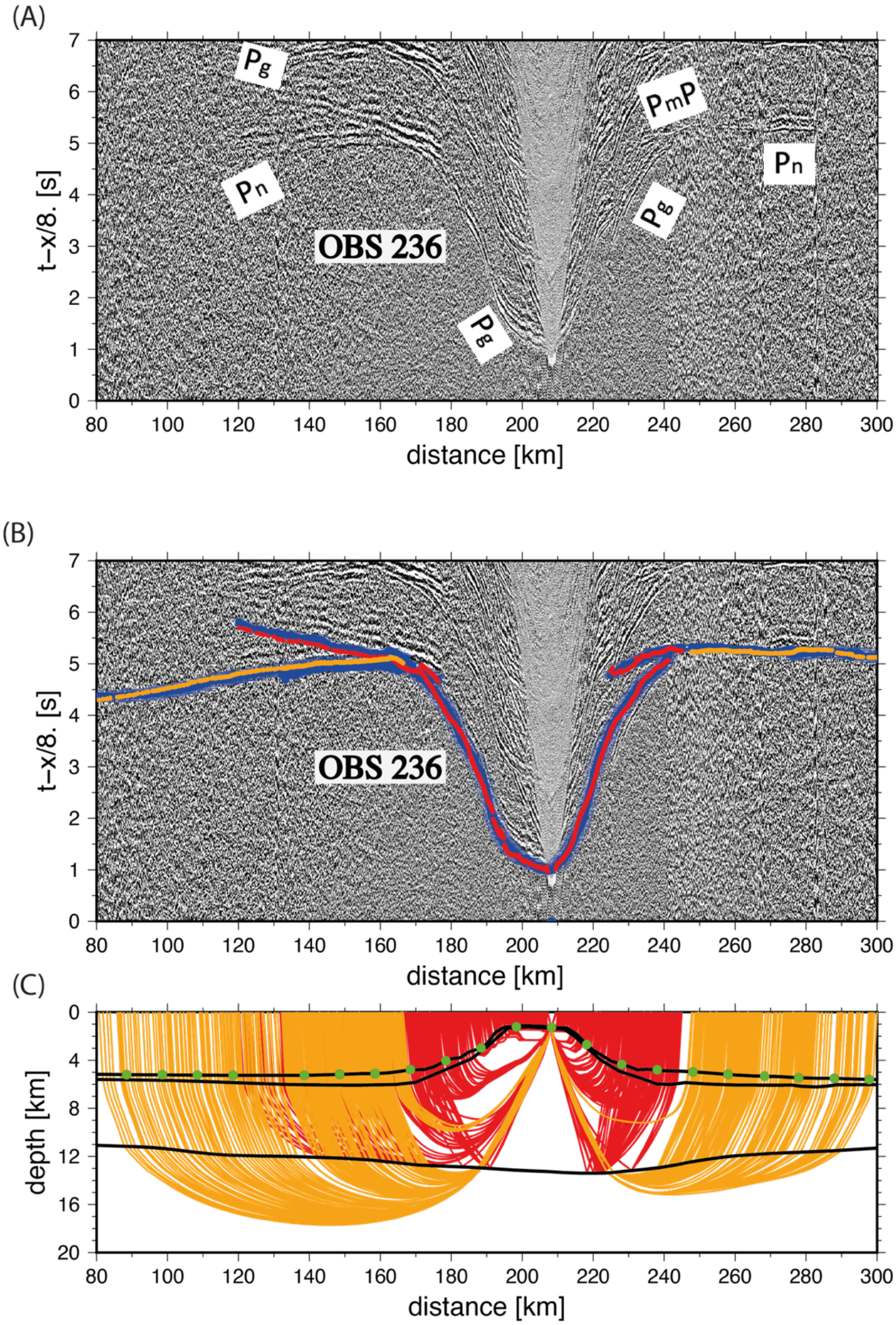

Fig. S3. (**A**) Wide-angle seismic data from OBH 236, plotted at a reduction velocity of 8 km/s and with crustal and mantle P-wave phases identified. (**B**) Predicted travel time are based on the 2-D V_p model shown in Fig. 7A. Blue bars corresponds to the travel time picks, scaled to the pick uncertainty. (**C**) Ray path diagram corresponding to the predicted travel times shown in (B). Green dots mark OBH/S locations.

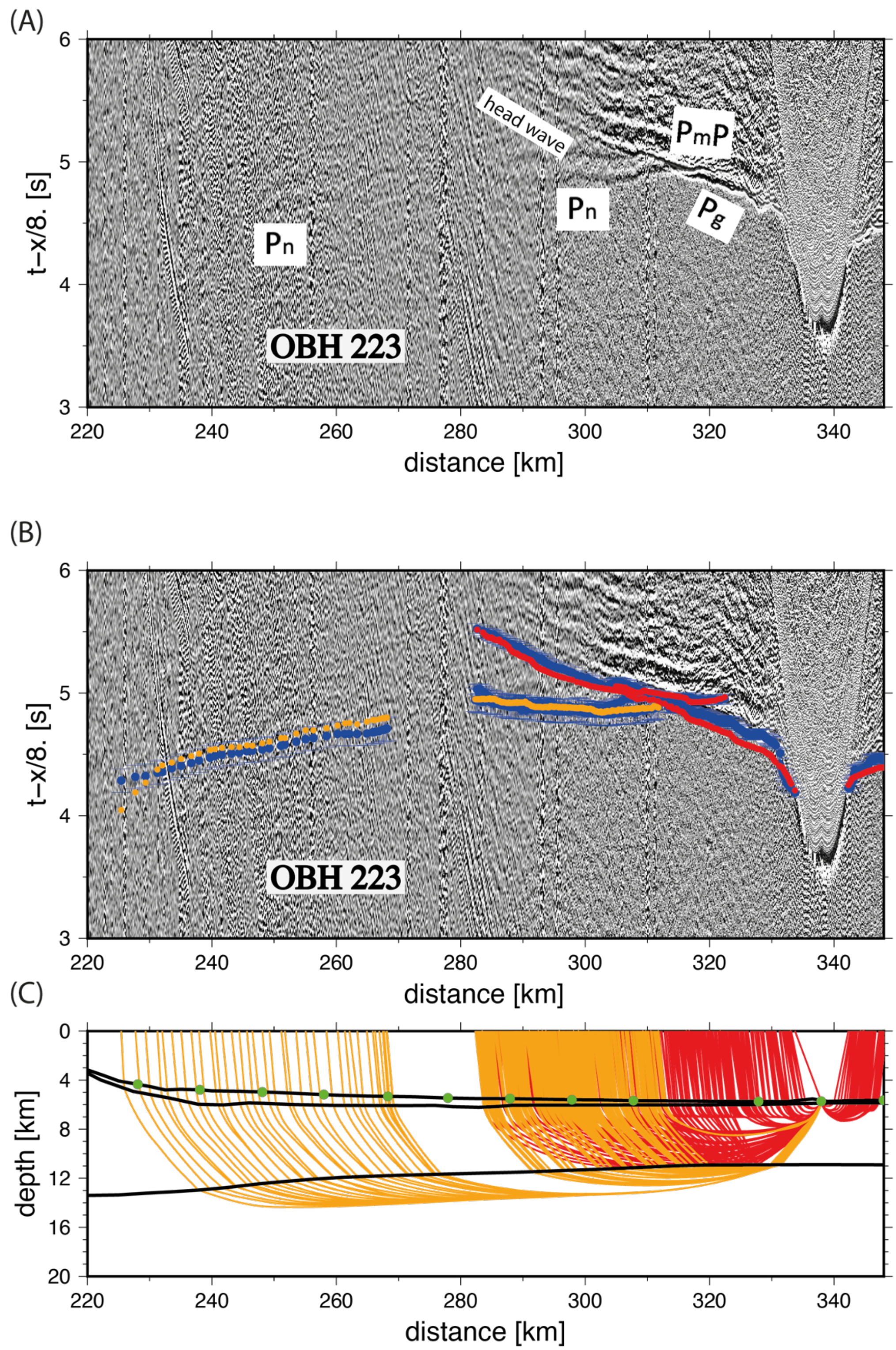

Fig. S4. (**A**) Wide-angle seismic data from OBH 223, plotted at a reduction velocity of 8 km/s and with crustal and mantle P-wave phases identified. (**B**) Predicted travel time are based on the 2-D V_p model shown in Fig. 7A. Blue bars corresponds to the travel time picks, scaled to the pick uncertainty. (**C**) Ray path diagram corresponding to the predicted travel times shown in (B). Green dots mark OBH/S locations.

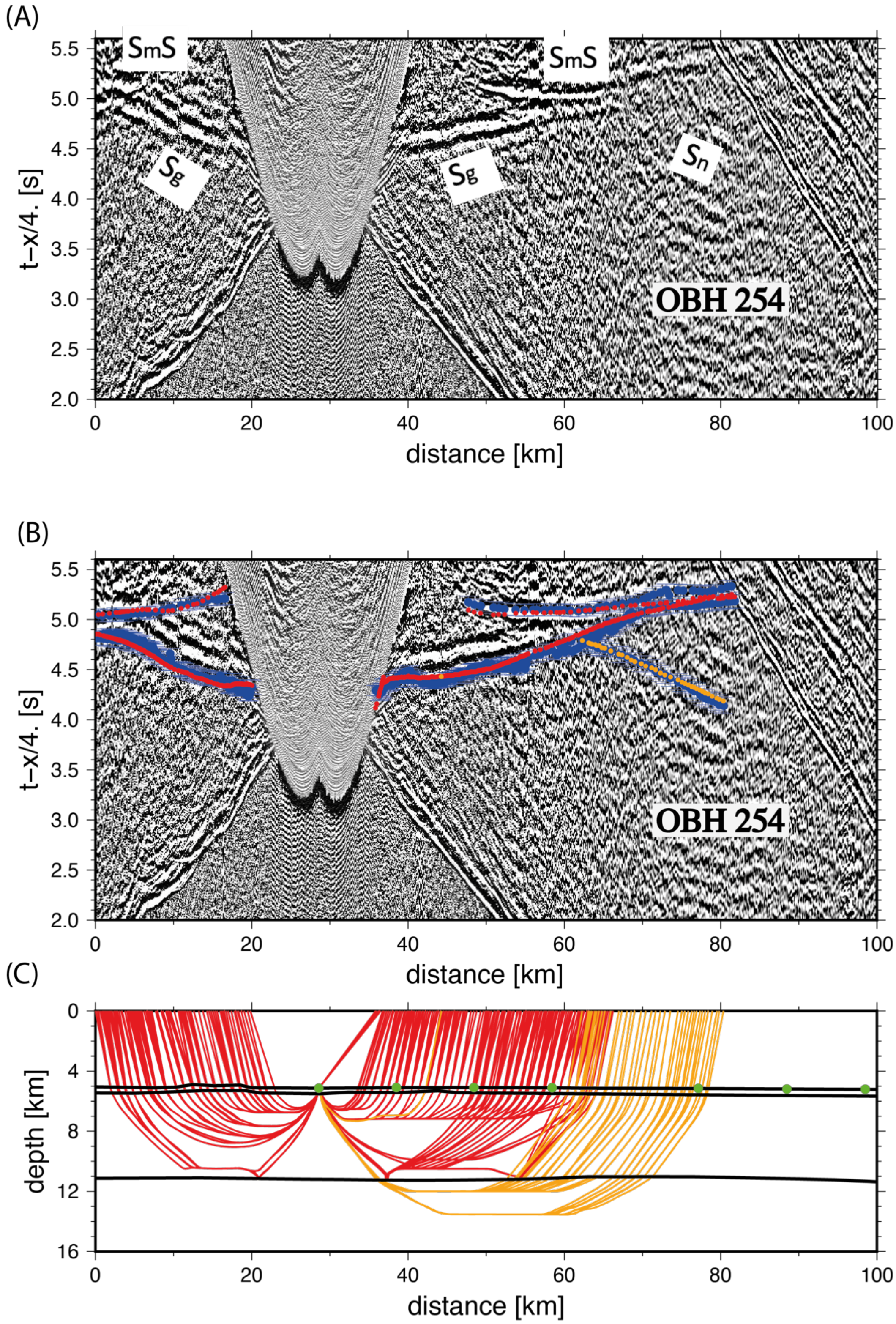

Fig. S5. (**A**) Wide-angle seismic data from OBH 254, plotted at a reduction velocity of 4 km/s and with converted S-wave phases identified. (**B**) Predicted travel time are based on the 2-D V_s model shown in Fig. 7B. Blue bars corresponds to the travel time picks, scaled to the pick uncertainty. (**C**) Ray path diagram corresponding to the predicted travel times shown in (B). Green dots mark OBH/S locations.

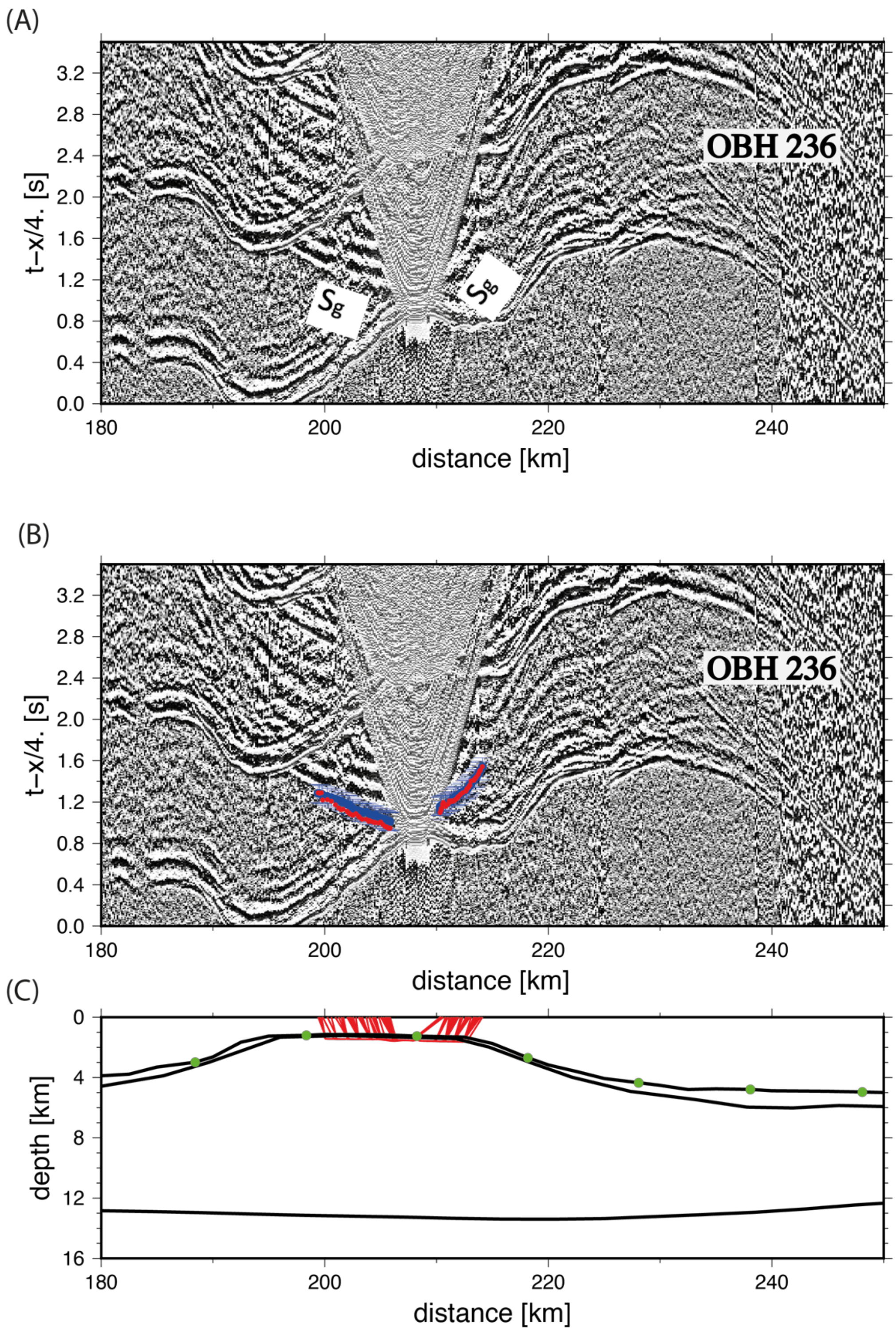

Fig. S6. (**A**) Wide-angle seismic data from OBH 236, plotted at a reduction velocity of 4 km/s and with converted S-wave phases identified. (**B**) Predicted travel time are based on the 2-D V_s model shown in Fig. 7B. Blue bars corresponds to the travel time picks, scaled to the pick uncertainty. (**C**) Ray path diagram corresponding to the predicted travel times shown in (B). Green dots mark OBH/S locations.

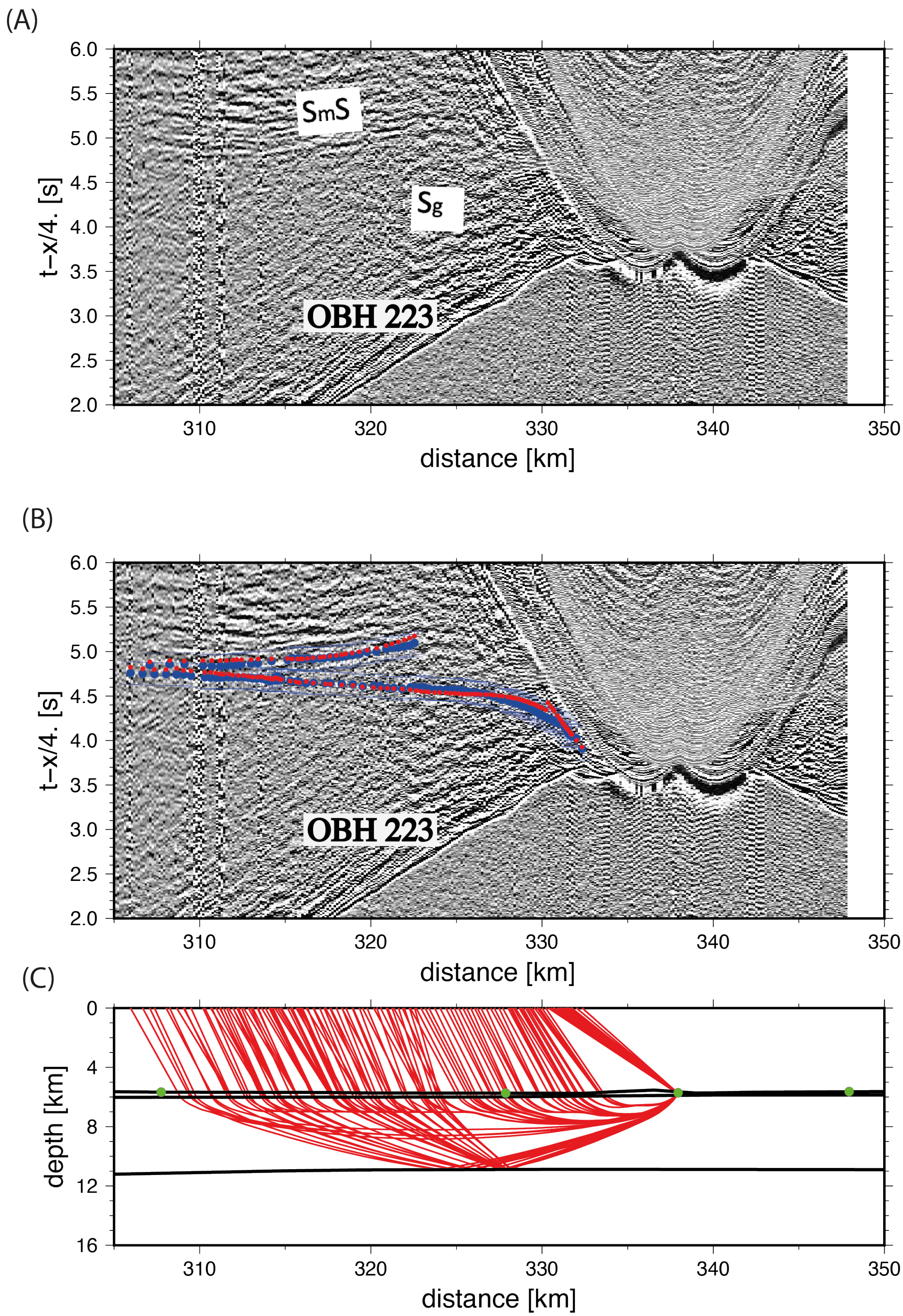

Fig. S7. (**A**) Wide-angle seismic data from OBH 223, plotted at a reduction velocity of 4 km/s and with converted S-wave phases identified. (**B**) Predicted travel time are based on the 2-D V_s model shown in Fig. 7B. Blue bars corresponds to the travel time picks, scaled to the pick uncertainty. (**C**) Ray path diagram corresponding to the predicted travel times shown in (B). Green dots mark OBH/S locations.

2. Seismic Modeling

The 2-D velocity structure that best fits the observed arrivals was determined using a joint refraction and reflection travel time inversion technique (Korenaga et al., 2000). This method allows the joint inversion of seismic refraction and reflection travel time data for a 2-D velocity field. Travel times and ray paths are calculated using a hybrid ray-tracing scheme based on the graph method and the local ray-bending refinement (van Avendonk et al., 1998). Smoothing constraints using pre-defined correlation lengths and optimized damping constraints for the model parameters are employed to regularize an iterative linearized inversion (Korenaga et al., 2000).

The best-fitting velocity model consists of the following layers: (1) water; (2) sediment/debris on top of the ridge; and (3) igneous crustal basement. To derive the velocity-depth model, the water depth was taken from the swath bathymetry center beam, and remained fixed during the inversion. The pelagic sedimentary layer was picked from the seismic reflection profile shown in Fig. 2 and then converted to depth assuming V_p = 1.7 km/s. The base of the flexural moat was taken from the final V_p tomographic model of Contreras-Reyes et al. (2010). To obtain the crustal P-wave velocities and the Moho depths, we jointly invert crustal refractions (P_g) and reflections (P_mP). To obtain the final model, we then inverted the mantle refractions (P_n). Moho depth is held fixed in the inversion of S-wave travel time picks.

3. Initial Model and Inversion Parameters

The 2-D velocity model is ~368 km long and 30 km deep. The initial model for P-wave tomographic inversion is based on the model of Contreras-Reyes et al. (2010). For the S-wave tomographic inversion, we based our initial model on the final P-wave model and converted it to S-wave velocity using a V_p/V_s ratio of 1.8 (Fig. S8). For both P-wave and S-wave velocity models, the horizontal grid spacing is 1 km, whereas the vertical grid spacing varies from 0.1 km at the top of the model to 0.15 km at the bottom. The horizontal correlation lengths range from 2 km at the top to 5 km at the bottom of the model, and the vertical correlation lengths vary from 0.5 km to 2 km, respectively. Depth nodes defining the Moho reflector are spaced at 4.5 km, with a correlation length of 4 km. The final average P-wave tomographic model is shown in Fig. 7A and the S-wave tomographic model in Fig. 7B. The root mean square (RMS) misfits are shown in Table S1.

Figs. S9-S14 show different checkerboard tests for the V_p and V_s models described in the main text in Section 3.3. Fig. S15 shows the Derivative Weight Sum (a proxy for the ray density), while Figs. S16 and S17 show the velocity uncertainties (as percentages) for the V_p and V_s models described in the main text in Section 3.4. Finally, Fig. S18 shows the 2-D V_p/V_s model and its percentage standard deviation.

Phase	Average travel time uncertainty (ms)	Final model T_{RMS} (ms)	Final model χ^2
$P_g + P_mP$	50-70	71	1.41
P_n	60	96	2.53
$S_g + S_mS$	70 – 90	82	1.89
S_n	70	129	4.61

Table S1. Travel-time misfit and data uncertainty for seismic profile P03. P_g: P-wave crustal refraction. P_mP: P-wave Moho reflection. P_n: P-wave mantle refraction. S_g: crustal S-wave refraction. S_mS: S-wave Moho reflection. S_n: S-wave mantle refraction. T_{RMS}: root-mean-square travel time misfit. χ^2: chi-square parameter.

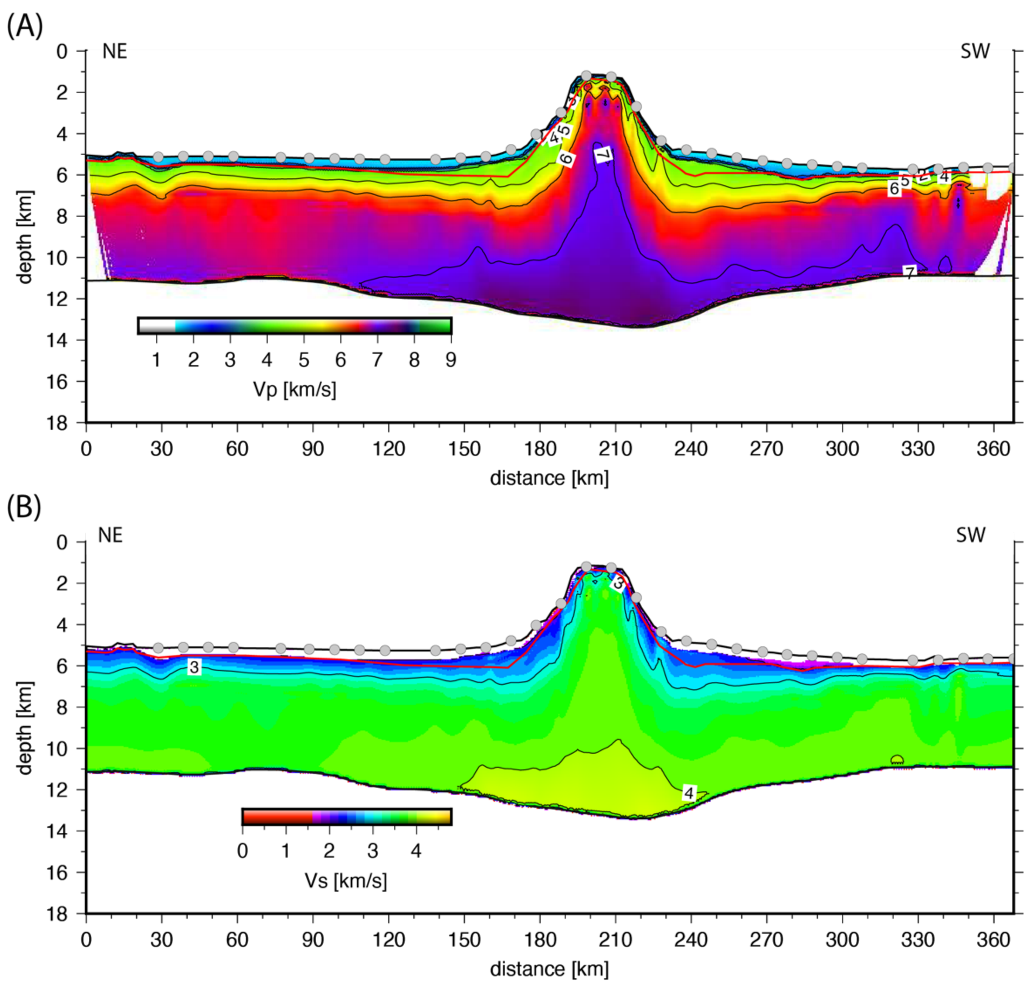

Fig. S8. (A) Two-dimensional V_p tomographic inversion model for the oceanic crust using P_g and P_mP phases (see Section 3.2). **(B)** Initial V_s tomographic model for the inversion of crustal S-wave travel time picks based on the V_p model shown in (A) and a V_p/V_s ratio of 1.8. Gray dots mark OBH/S locations.

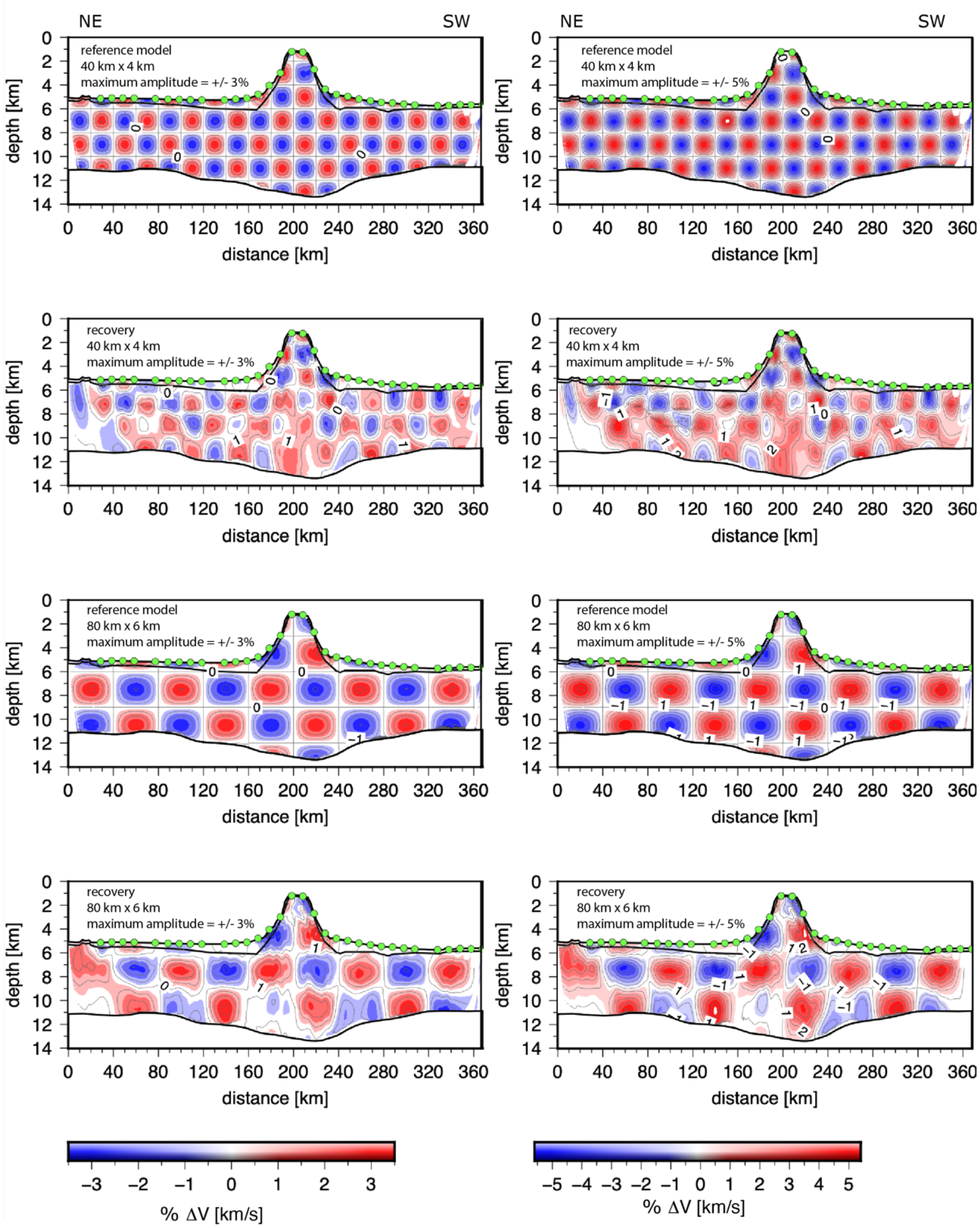

Fig. S9. Results of checkerboard tests for the oceanic crust of the V_p model. The synthetic reference velocity models have ±3% and ±5% velocity anomalies of different sizes (as annotated) applied. Green dots mark OBH/S locations.

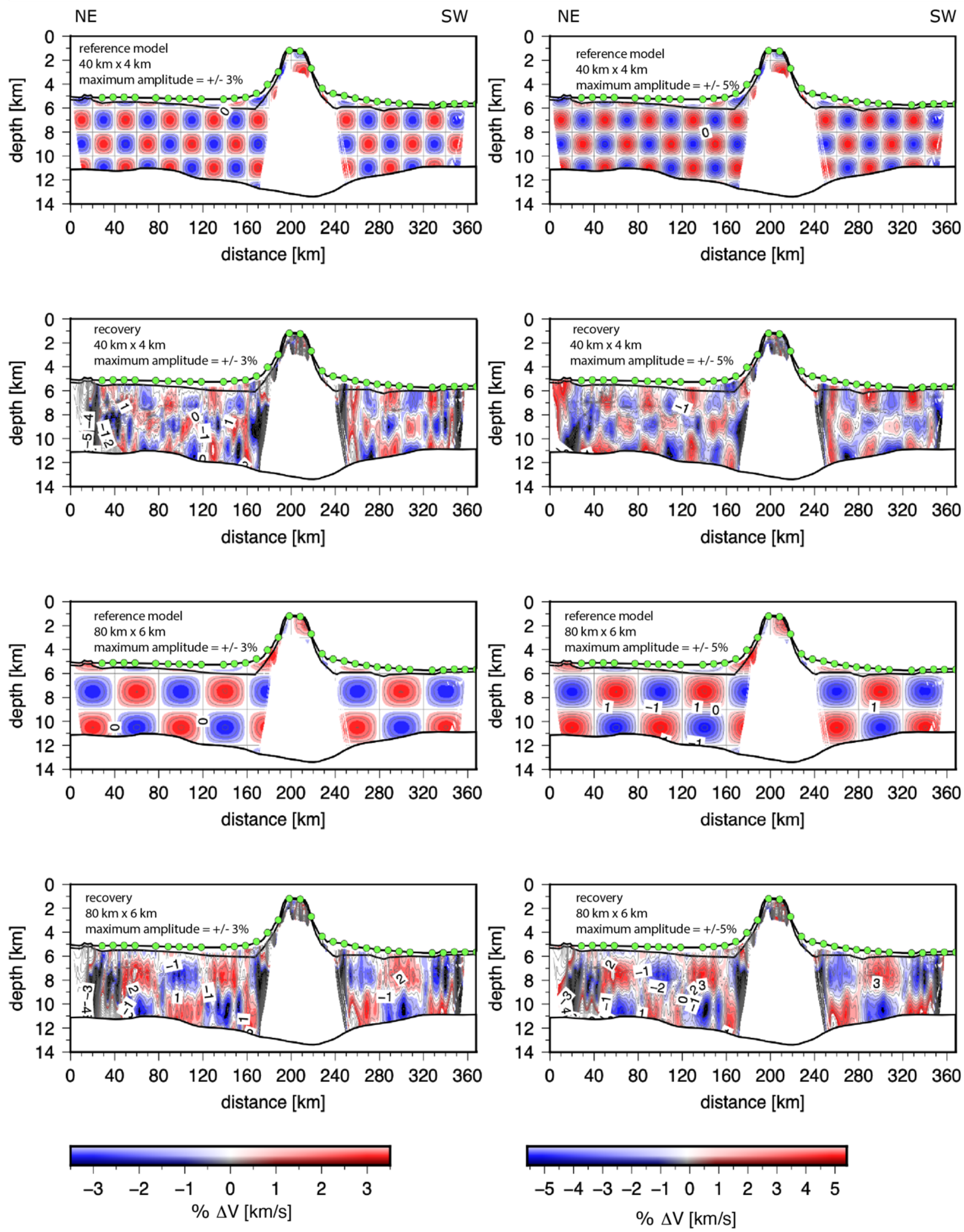

Fig. S10. Results of checkerboard tests for the oceanic crust of the V_s model. The synthetic reference velocity models have ±3% and ±5% velocity anomalies of different sizes (as annotated) applied. Green dots mark OBH/S locations.

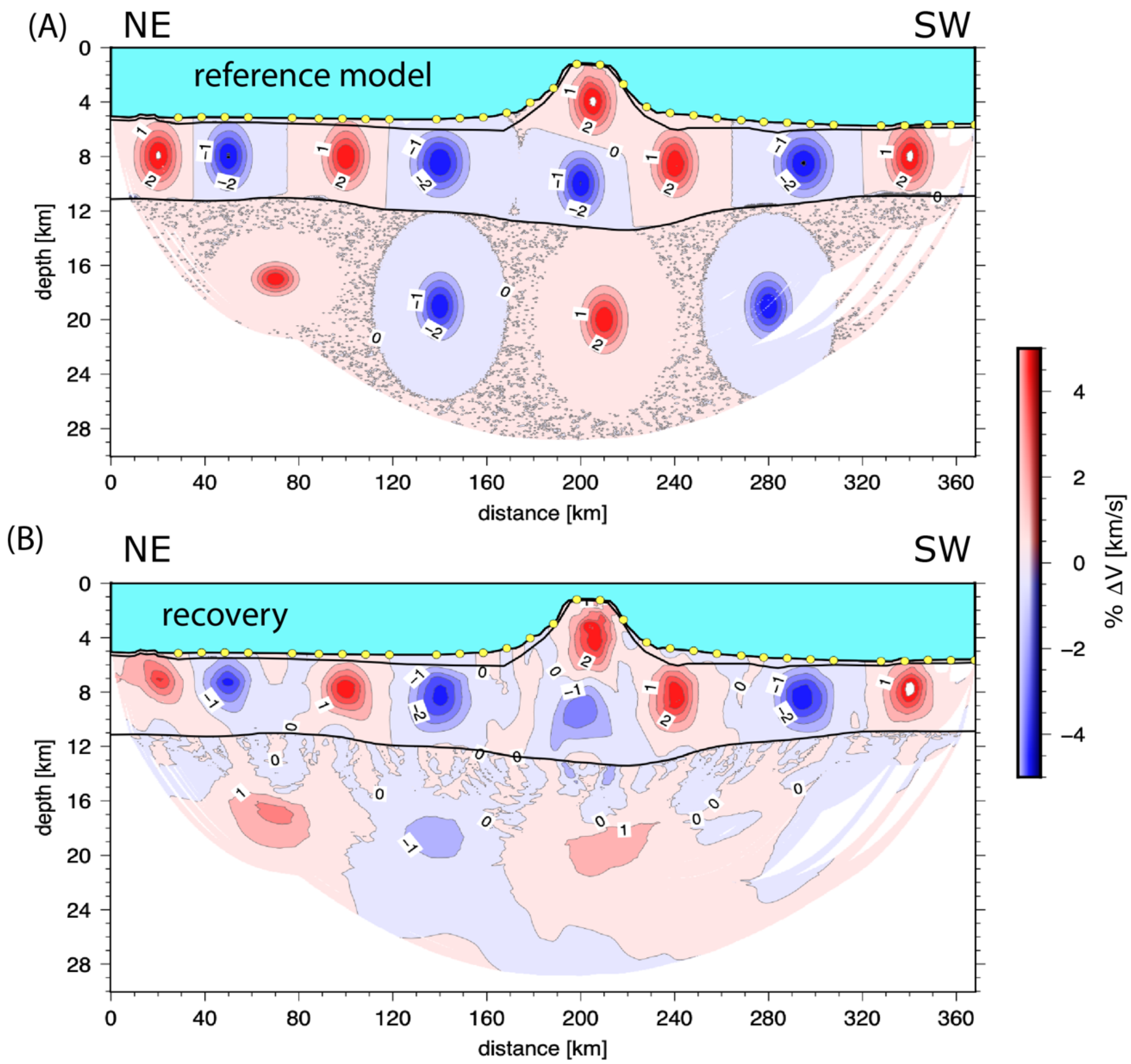

Fig. S11. (A) Synthetic V_p reference velocity-depth model consisting of of ±5% Gaussian anomalies (40 km *x* 8 km and 40 km *x* 14 km in the crust and mantle, respectively) superimposed onto the final P-wave velocity model shown in Fig. 7A. **(B)** Recovery for the V_p model using the same instrument geometry and ray density (see Section 3.3). Yellow dots mark OBH/S locations.

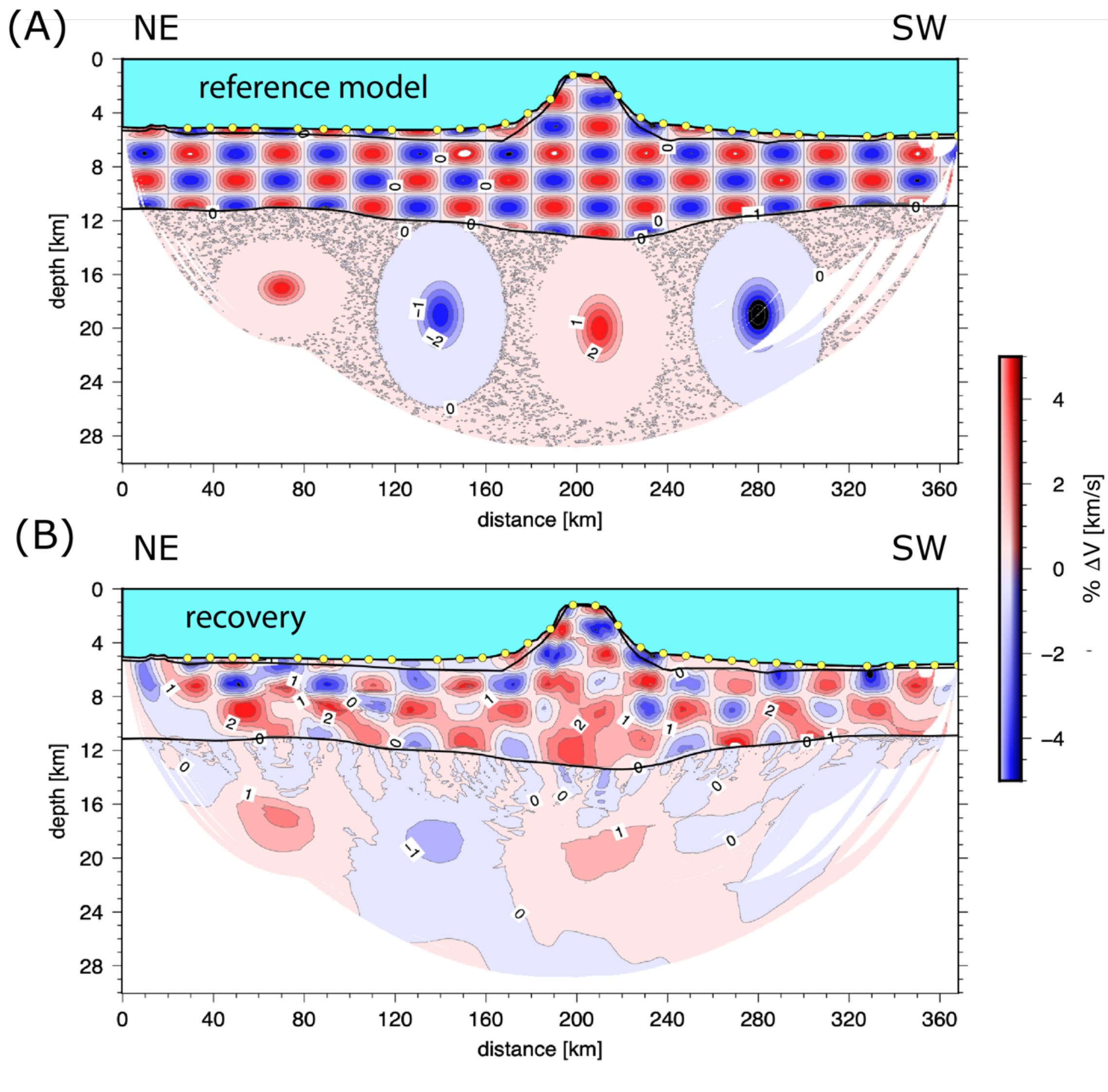

Fig. S12. (A) Synthetic V_p reference velocity-depth model consisting of ±5% Gaussian anomalies (20 km *x* 2 km and 40 km *x* 14 km in the crust and mantle, respectively) superimposed onto the final P-wave velocity model shown in Fig. 7A. **(B)** Recovery for the V_p model using the same instrument geometry and ray density (see Section 3.3). Yellow dots mark OBH/S locations.

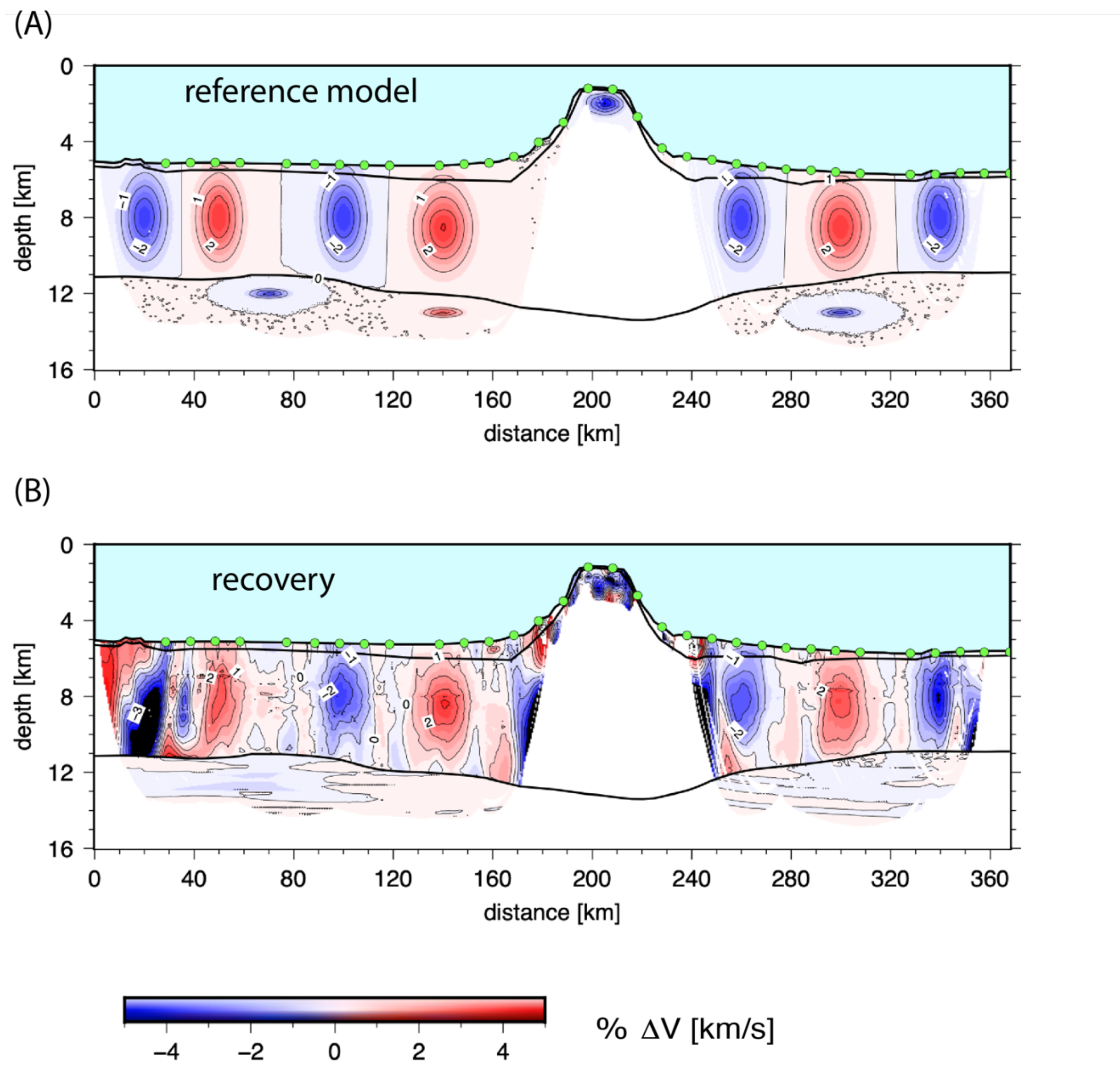

Fig. S13. (A) Synthetic V_s reference velocity-depth model consisting of ±5% Gaussian anomalies (40 km *x* 8 km and 40 km *x* 4 km in the crust and mantle, respectively) superimposed onto the final S-wave velocity model shown in Fig. 7B. **(B)** Recovery for the V_s model using the same instrument geometry and ray density (see Section 3.3). Green dots mark OBH/S locations.

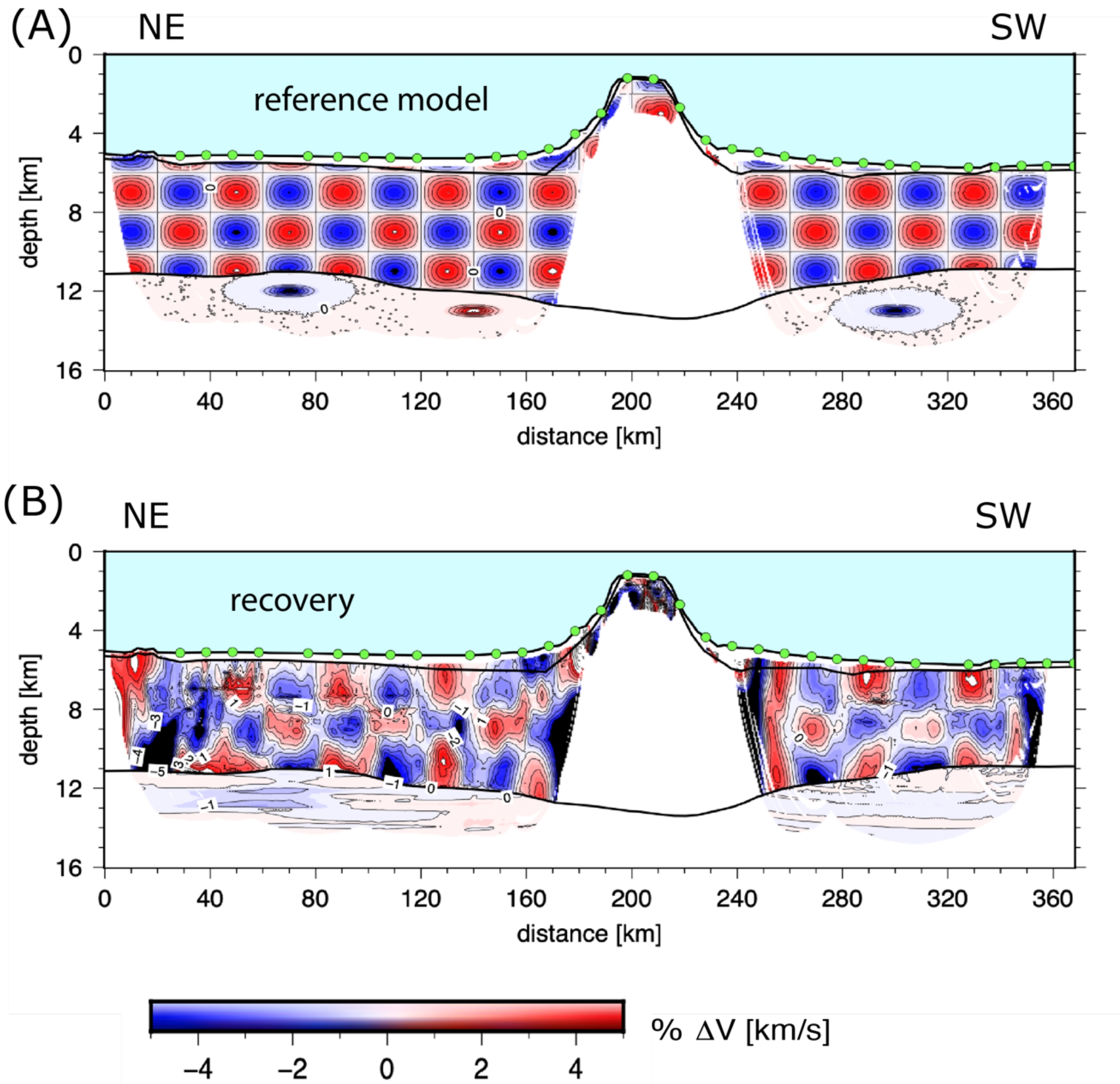

Fig. S14. (A) Synthetic V_s reference velocity-depth model consisting of ±5% Gaussian anomalies (20 km *x* 2 km and 40 km *x* 4 km in the crust and mantle, respectively) superimposed onto the final S-wave velocity model shown in Fig. 7B. **(B)** Recovery for the V_s model using the same instrument geometry and ray density (see Section 3.3). Green dots mark OBH/S locations.

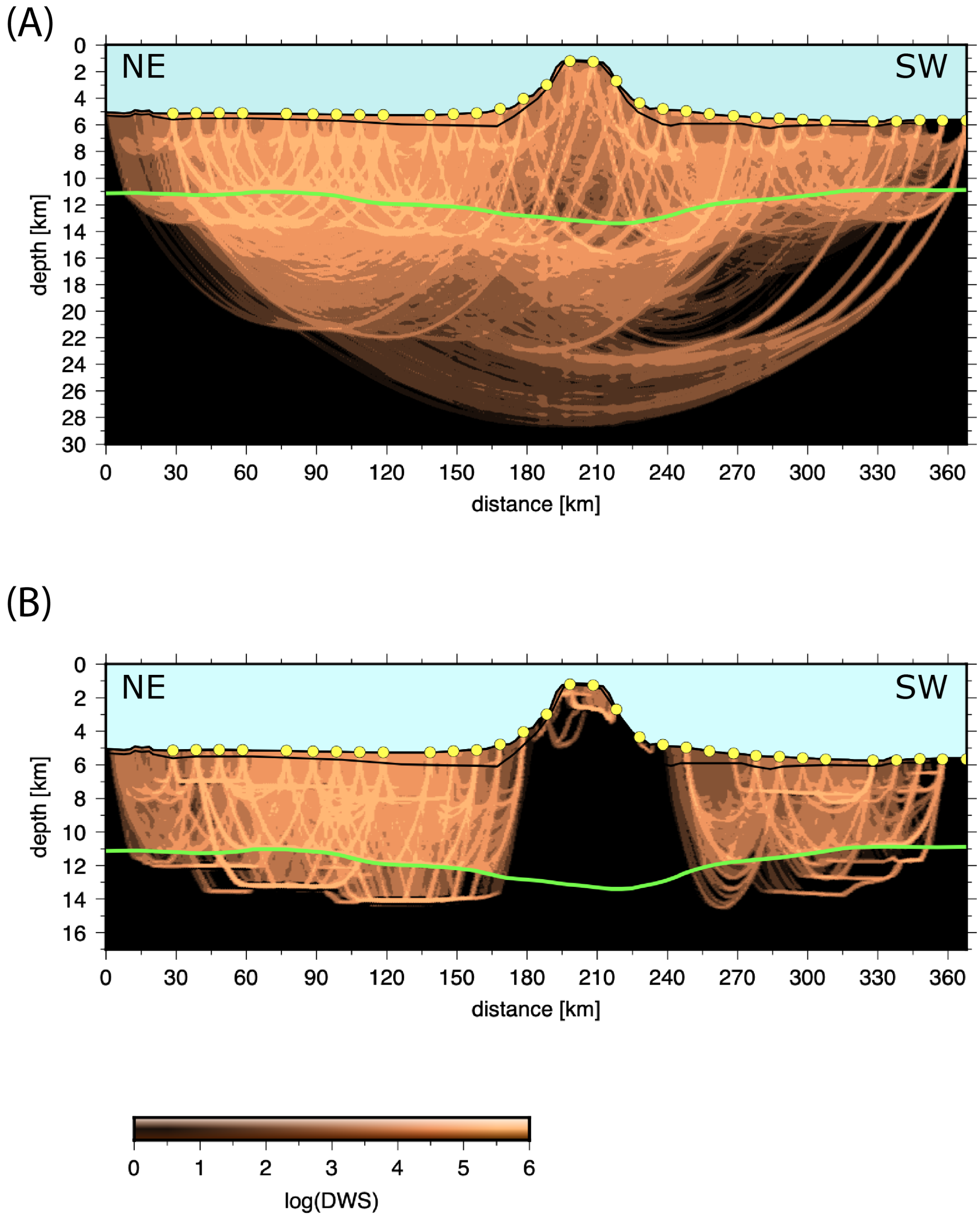

Fig. S15. DWS for rays traveling through the **(A)** V_p and **(B)** V_s models plotted using a logarithmic scale. Yellow dots mark OBH/S locations.

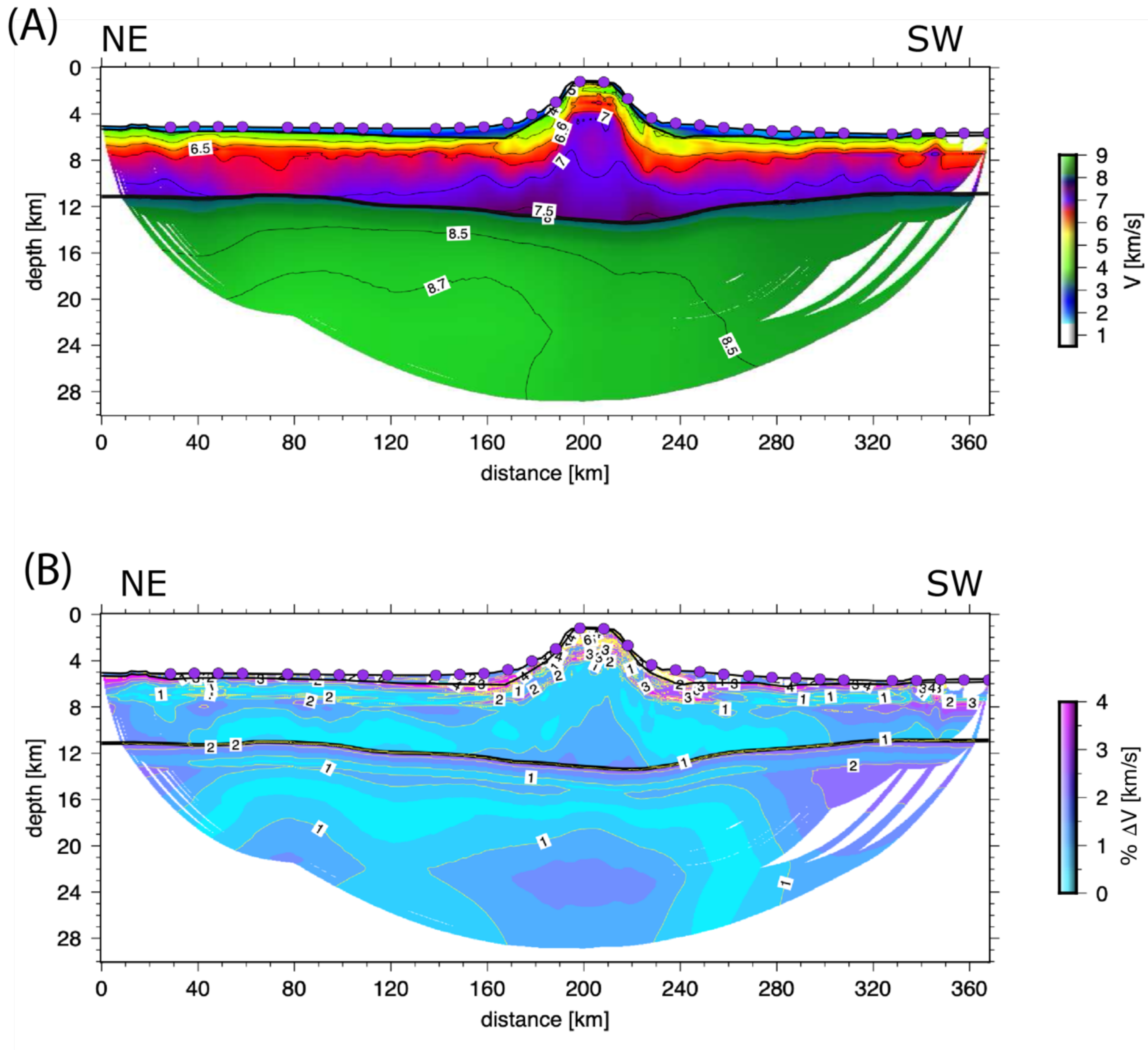

Fig. S16. (**A**) Average P-wave velocity model. **(B)** Percentage standard deviation model (ΔV) of the V_p model (see Section 3.4). Green dots mark OBH/S locations.

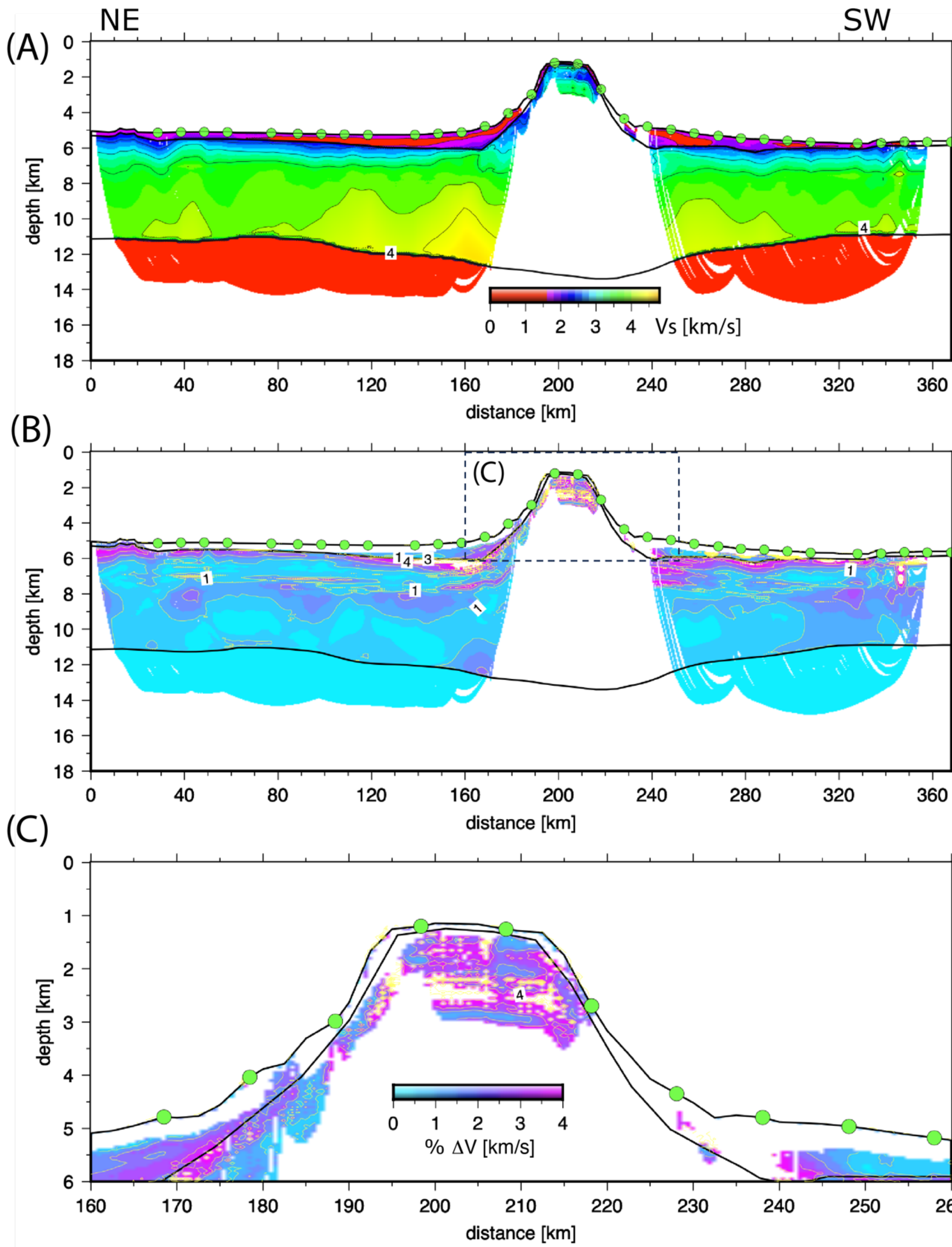

Fig. S17. (**A**) Average S-wave velocity model. **(B)** Percentage standard deviation model (ΔV) of the V_s model (see Section 3.4). **(C)** Zoom-in of the summit region shown in (B).

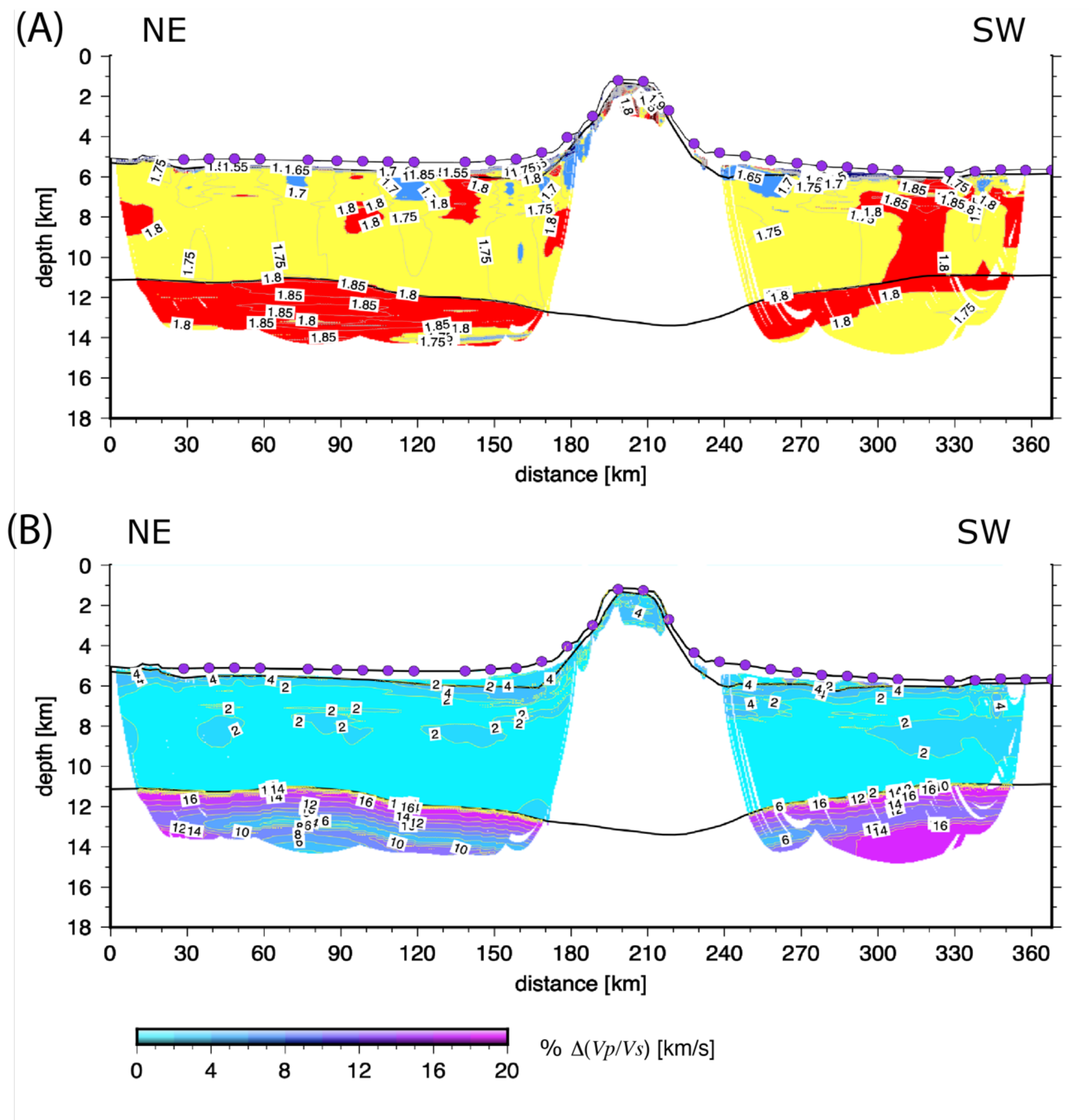

Fig. S18. (A) Derived 2-D V_p/V_s model based on the V_p and V_s model shown in Figs. S16A and S17A. **(B)** Percentage standard deviation model $100x\frac{\Delta(Vp/Vs)}{Vp/Vs}$ where $\Delta(Vp/Vs)$ is calculated using Eq. 1 (see Section 3.4). Purple dots mark OBH/S locations.

References cited in the Supporting Information

Contreras-Reyes, E., Grevemeyer, I., Watts, A. B., Planert, L., Flueh, E. R., & Peirce, C. (2010). Crustal intrusion beneath the Louisville hotspot track. *Earth and Planetary Science Letters*, *289*(3-4), 323-333.

Grevemeyer I., and Flueh E. (2008), FS Sonne SO195 cruise report: Tonga thrust earthquake asperity at Louisville ridge (TOTAL), 2008, pg. 101.

Korenaga, J., Holbrook, W. S., Kent, G. M., Kelemen, P. B., Detrick, R. S., Larsen, H.-C., et al. (2000). Crustal structure the southeast Greenland margin from joint refraction and reflection seismic tomography. *J. Geophys. Res.*, 105(B9), 21,591–21,614. https://doi.org/10.1029/2000JB900188

Van Avendonk, H. J., Harding, A. J., Orcutt, J. A., and McClain, J. S. (1998), A two-dimensional tomographic study of the Clipperton transform fault. *J. Geophys. Res.: Solid Earth*, *103*(B8), 17885-17899. doi:10.1029/98JB00904.

White, R. S., and Stephen, R. A. (1980). Compressional to shear wave conversion in oceanic crust. *Geophys. J. Int.*, *63*(2), 547-565.